Final Report
NOAA Grant 04-8-MO
March 1, 1978 to December 31, 1979

Use of Environmental Satellite Data for Input to Energy Balance Snowmelt Models

Washington, DC
December 1980

U.S. DEPARTMENT OF Commerce
National Oceanic and Atmospheric Administration
National Earth Satellite Service

USE OF ENVIRONMENTAL SATELLITE DATA FOR INPUT TO ENERGY BALANCE SNOWMELT MODELS

Principal Investigator
Jeff Dozier

Final Report
NOAA Grant 04-8-M0
March 1, 1978 to December 31, 1979

Computer Systems Laboratory
University of California
Santa Barbara, CA 93106
Report TR-CSL-8001

ABSTRACT

This document describes the tasks completed during the tenure of the grant. Accomplishments include development of solar and longwave radiation models for alpine snow covered terrain, techniques for atmospheric correction of satellite radiometric data and for snow albedo determination from satellite, a very fast solution to the terrain horizon problem, investigations of the use of NOAA satellite data for snow surface temperature mapping, and work on canopy cover measurements from satellite for use in solar and longwave radiation models.

USE OF ENVIRONMENTAL SATELLITE DATA FOR INPUT TO ENERGY BALANCE SNOWMELT MODELS

Principal Investigator
Jeff Dozier

Final Report
NOAA Grant 04-8-M0
March 1, 1978 to December 31, 1979

Computer Systems Laboratory
University of California
Santa Barbara, CA 93106
Report TR-CSL-8001

Specific Accomplishments

1. An instrument system for ground truth data collection for satellite snow studies has been developed and installed. One essential component of this system is a remote micrometeorological station which we have operated as a satellite data collection platform. Performance of the system under isolated alpine conditions has been satisfactory.

2. Models for clear sky solar and longwave radiation have been developed and tested.

3. The clear sky solar radiation model has been extended to calculate the necessary corrections for satellite radiometric data over rugged terrain.

4. A method for satellite determination of snow albedo has been developed and tested.

5. A very fast (order N) algorithm for computing horizon profiles over a digital terrain grid has been developed.

6. Comparisons of field temperature data with the thermal channel of TIROS-N indicate that satellite mapping of snow surface temperature is feasible.

7. Extensive point measurements of forest canopy densities have been made during both winter and summer conditions. These will be extended over the study area by correlation to satellite brightness data. This information will then be used to model the effect of canopy

cover on the snow surface radiation budget.

Instrumentation

A satellite data collection platform (DCP) was purchased from the LaBarge Corp. It was delivered to us in December 1978, after the snow season had begun, and was installed for the 1979 snow season at Horseshoe Meadow, in the Owens River drainage but only 2 km from the drainage divide with the Kern River. The 1979 season was essentially used as a "debugging" period for this instrument, and several problems and malfunctioning components were corrected.

Since October 1979 the DCP has been operating at Charlotte Ridge, at an elevation of 3328 m between Charlotte and Bullfrog Lakes in the Kings River drainage, South Fork. The data collection interval is 30 min; the transmission interval is 6 hr. The instrument array includes:

Eppley precision spectral pyranometer (.28 to 2.8 Mm) - pointed up. Used for measurement of total incoming solar radiation and consequent calibration of solar radiation model.

Eppley precision spectral pyranometer with RG-8 filter (.7 to 2.8 Mm) - pointed up. Used for measurement of incoming solar radiation in near-infrared spectral region and consequent calibration of solar radiation model.

Eppley pyrgeometer (4 to 50 Mm) - pointed up. Used for measurement of incoming longwave radiation.

Met One ambient air temperature sensor.

Met One relative humidity sensor.

Met One wind velocity sensor.

snow/soil interface temperature sensor.

We also have a more complete instrumentation site at Mammoth Mountain, which we have operated in cooperation with the U.S. Forest Service. For the 1979-80 snow season we have purchased a digital recorder (using funds from the California Space Institute) so that data can be recorded at 5 min intervals. The following instruments are connected to this recorder:

2 Eppley precision spectral pyranometers (.28 to 2.8 Mm) - one pointed up and one pointed down. Used for measurement of incoming and reflected radiation in total solar spectral range.

2 Eppley precision spectral pyranometers with RG-8 filters (.7 to 2.8 Mm) - one pointed up and one pointed down. Used for measurement of incoming and reflected radiation in near-infrared spectral range.

2 Eppley pyrgeometers (4 to 50 Mm) - one pointed up and one pointed down. Used for measurement of incoming longwave radiation and snow surface temperature.

Very accurate condensation mirror device for measurement of dew point temperature.

Air temperature sensor.

In addition the Mammoth instrumentation site has fixed interval thermistor arrays to provide a snow/soil temperature profile at 15 cm resolution. These are read manually every day. Six runoff collection pans totalling 10 sq m of surface area provide measurements of water drainage at the bottom of the snow pack.

Publications

The following papers have appeared in print. Five copies of each of these have been supplied with this report.

1. Dozier, J., 1979, A solar radiation model for a snow surface in mountainous terrain, in Proceedings, Modeling of Snow Cover Runoff, S.C. Colbeck and M. Ray, editors, U.S. Army Cold Regions Research and Engineering Laboratory, pp. 144-153.

2. Marks, D., 1979, An atmospheric radiation model for general alpine application, in Proceedings, Modeling of Snow Cover Runoff, S.C. Colbeck and M. Ray, editors, U.S. Army Cold Regions Research and Engineering Laboratory, pp. 167-178.

3. Marks, D., and Dozier, J., 1979, A clear-sky longwave radiation model for remote alpine areas, Archiv fur Meteorologie Geophysik und Bioklimatologie, ser. B., 27, 159-187.

4. Dozier, J., A clear-sky spectral solar radiation model for snow-covered mountainous terrain, Water Resources Research, 16, 709-718.

The following manuscripts have been accepted for publication. Copies of the abstracts are included below, but copies of the papers themselves have not been included as part of the final report. When they actually appear in print, five copies of each shall be furnished to the Technical Monitor.

1. Dozier, J., Bruno, J., and Downey, P., A faster solution to the horizon problem, to appear in Computers and Geosciences.

   We develop an algorithm for calculating the horizons for each point in a digital terrain grid in order N iterations, whereas all previous methods seem to be of order N squared time complexity. The new method makes horizon computations reasonable, and ought to improve the accuracy of surface climate models in rugged terrain.

2. Frampton, M.F., and Marks, D., Mapping snow surface temperature from thermal satellite data in the Southern Sierra Nevada, Proceedings of the 1980 Western Snow Conference, to appear.

   Mapping snow surface temperature over a large alpine area is a useful tool for snowmelt runoff investigations. Tiros-N satellite data are used to measure snow surface temperature over a large area. These measurements have been corrected for atmospheric and terrain effects, and are used to calibrate an energy balance snowmelt model under development. The satellite data are calibrated with micrometeorological data from two remote stations in the southern Sierra Nevada, and from active field measurement of snow surface temperature using a radiant thermometer. Data products from the satellite temperature measurements include a temperature grid for wind flow modeling, temperature contouring and a quantitative measure of snow surface temperature regimes, and thermal inertia data for remote determination of average snow density.

3. Marks, B., and Marks, D., Areal determination of the influence of a forest canopy on the surface radiant energy exchange, Proceedings of the 1980 Western Snow Conference, to appear.

   To accurately model the energy balance of an alpine snowpack, the influence of a vegetation canopy on the surface radiant energy exchange must be known. A number of studies have been conducted to determine the shading effects of a canopy at a point. This paper presents a new method of estimating canopy cover density which can be extended over a large area. Canopy shading functions, developed from photographic techniques, describe the proportion of the hemisphere surrounding a point which is partially obscured by vegetation. A general diffuse shading function, and a beam shading function which accounts for changes in solar zenith are presented. Both functions account for changes in canopy cover density with variations in snow depth. A combination of Landsat satellite data and

field measurements are used to extend the estimated canopy densities over a large area of the southern Sierra Nevada. The shading functions can then be used in areal models of solar and terrestrial radiation.

The following manuscripts have been completed, but have not yet been accepted for publication in the refereed literature. Copies are included as part of this final report.

1. Dozier, J., and Frew, J.E., Atmospheric corrections to satellite data over rugged terrain, submitted to Remote Sensing of Environment.

2. Frew, J., Remote sensing of snow surface albedo, M.A. thesis, University of California.

Software

A useful product of our research has been the development of an extensive system of programs for integrating numerous types of satellite data and NCIC digital terrain data with models of surface processes. The programs and functions have been written and tested on a small computer, a PDP-11/45 with Unix operating system, and most of them have been transferred to a VAX-11/780 under Version 7 of Unix. All routines are in the C language.

The widespread utility and portability of these programs is limited at present. The C language is available on only a few machines, although a portable compiler has been written (but not yet released). Its major advantages are that it allows the user to write efficient, readable, structured code and that it virtually eliminates the need for the ordinary user to resort to assembly language. In the future, as the Unix system and the C language become more widely available and as operational installations acquire more advanced and more efficient interactive operating systems, the distribution of these programs will be useful. It is worth noting that Amdahl has developed a Unix system for their in-house machine, and that IBM is working on a micro-processor interface so that Unix can be installed on their new 4300 series computers.

Unfinished Projects

1. We have not fully investigated the implications of snow surface temperature and its relation to snowmelt runoff. Due to the late delivery of Tiros-N data, and to the fact that the West Coast data were available only in field station format, our work on this phase proceeded far more slowly than we expected. In particular, the geometric rectification and registration of the data using ground control points was time-

consuming.

2. We have not examined the differences in measured snow reflectance due to scale differences in Landsat MSS vs NOAA satellite data.

3. We have made only an initial start to using thermal satellite data as part of a terrain wind model.

ATMOSPHERIC CORRECTIONS TO SATELLITE RADIOMETRIC DATA OVER RUGGED TERRAIN

Jeff Dozier and James Frew
Department of Geography
University of California
Santa Barbara, CA 93106

for
Remote Sensing of Environment

Abstract

Radiometric measurements from satellites in the solar portion of the electro-magnetic spectrum can be converted to measurements of surface exitance. Over rugged terrain, the satellite image must be precisely registered to a terrain data set. For small areas a first-order polynomial interpolation scheme is generally satisfactory for the geometric rectification. Because of the widespread existence of saturated pixels, a nearest-neighbor procedure is used for the interpolated satellite radiance numbers. Path radiance and path transmission are calculated with a simple spectral model, which requires an estimate of the water vapor and aerosol content of the atmosphere.

Notation

a/Re	absorptance/reflectance ratio for atmospheric aerosols
EO	solar constant
Ed	diffuse irradiance
Es	direct (beam) irradiance
E′	irradiance scattered out of incoming beam
ko	ozone absorption coefficient
kw	water vapor absorption coefficient
L	radiance
M	exitance
M′	surface exitance which is subsequently scattered
ma	optical air mass
(O3)	atmospheric ozone content (mm)
P	air pressure (Pa)
r	earth-sun radius vector
RN	satellite radiance number
w	precipitable water vapor (mm)
z	altitude (m)
Z	solar zenith angle
α	Angstrom turbidity exponent
β	Angstrom turbidity coefficient
λ	wavelength
ρ	surface diffuse reflectance to direct irradiance
ρ'	surface diffuse reflectance to diffuse irradiance
σA	aerosol attenuation coefficient
σR	Rayleigh scattering coefficient
τ	atmospheric transmissivity

Introduction

Space-borne radiometers which measure upwelling radiance in the solar portion of the electro-magnetic spectrum can be used to estimate the spatial distribution of surface parameters which are useful in calculating the surface energy budget. In order to properly use the measurements, it is necessary to derive the radiant exitance from the earth's surface. Hence calculation of the atmospheric path radiance and the atmospheric attenuation of the upwelling surface radiance are necessary. Over terrain of varying elevation, it is generally not true that these quantities are unchanging over the area of interest, so precise registration of the satellite radiometric data with the underlying terrain is necessary.

The method presented herein is based upon a simple spectral solar radiation model, with Rayleigh and aerosol scattering and absorption from aerosols, water vapor, and ozone. Necessary parameters to drive the model are derived from surface measurements (Dozier, 1980).

Background

Upwelling monochromatic space radiance at the top of the atmosphere has two sources: (1) upward scattering of solar radiation and (2) solar radiation reflected from the surface and subsequently transmitted back through the atmosphere:

$$L\uparrow[\lambda]space = L\uparrow[\lambda]path + \tau[\lambda]\, M[\lambda]surf / \pi \qquad (1)$$

where

$$M[\lambda]surf = \rho'[\lambda]\ Ed[\lambda] + \rho[\lambda]\ Es[\lambda] \qquad (2)$$

Complications in applying equations (1) and (2) are:

1. Most space-borne radiometers (e.g. Landsat) are not monochromatic, but measure integrated upwelling space radiance within some broad wavelength band(s).

2. $L\uparrow[\lambda]path$ varies with the altitude of the surface, the atmospheric attenuation parameters, and the solar angle.

3. The transmission function $\tau[\lambda]$ for upwelling radiance includes attenuation for scattering and absorption. Some of the scattered radiation arrives at the top of the atmosphere over nearby pixels instead of over the pixel from which it left the surface. Moreover $\tau[\lambda]$ varies with the altitude of the surface.

4. Surface reflectances $\rho'[\lambda]$ and $\rho[\lambda]$ are functions of wavelength, and $\rho[\lambda]$ is also a function of illumination angle. Moreover, the spectral distribution of $M[\lambda]$ is a convolution of the spectral distributions of irradiance and reflectance.

Preprocessing of Satellite Radiometric Data

If satellite radiometric data are to be used to derive $L_{\uparrow}[\lambda]_{path}$, they must first be subjected to certain radiometric and geometric transformations. These transformations are collectively described as "preprocessing" since they are a prerequisite to the extraction of usable information. There are two principal requirements which the preprocessing of satellite radiometric data must fulfill:

1. The data must be converted from their original representation (e.g. digital quantization levels) into measures of radiant power intensity.

2. Each spaceborne measurement must be correlated with an earth surface location, to account for the influence of spatially varying surface characteristics on the terms in equations (1) and (2).

How the preprocessing is implemented is contingent upon the radiometric and geometric characteristics of the particular sensor system from which the data are obtained. In this section, we discuss the relevant characteristics of the Landsat multispectral scanner (MSS) system, and then describe the preprocessing scheme by which we convert these data to space radiance measurements.

In the radiometric domain, spectral radiance levels detected by the MSS are spatially sampled and quantized at 6-bit resolution (and expanded to 7-bits upon CCT generation for bands 4, 5, and 6) (NASA, 1976). This leads to the representation of a scene as an array of integer radiance numbers (RNs), ranging from 0 to

127 (0 to 63 for band 7). Ideally, the point-by-point conversion of these RNs into space upwelling radiances is accomplished by the following linear transform:

$$L\uparrow[\lambda]space = (RN[\lambda] / RN[\lambda]max) (L[\lambda]sat - L[\lambda]thresh) + L[\lambda]thresh \quad (3)$$

In practice, the conversion is complicated by response variations between the six detectors in a given band (causing the notorious "striping" observable on many MSS images), and by the presence of threshold (RN = 0) and saturated (RN = 63 or 127) pixels over the area of interest. Inter-detector response variations can be dealt with by statistical equalization, based on either an analysis of a single scene (Landgrebe et al., 1974; Bernstein and Ferneyhough, 1975), or on a multi-temporal analysis of several scenes (Potter, 1977). Statistical equalization is an effective method of "smoothing" radiometric errors, but it is undesirable for radiation studies since the original RN-to-radiance transforms would no longer be usable.

Threshold and saturated pixels are a problem in radiation studies since they cannot be assigned radiance levels based on the linear transform described above. In the case of threshold pixels, it is known only that the corresponding radiance is less than or equal to the threshold response of the sensor. Similarly, saturated pixels may represent any value greater than or equal to the saturation level of the sensor. Saturation especially is a significant problem over areas of very high surface reflectance. For example, we have noted 20 to 40 percent

saturation in MSS bands 4, 5, and 6 over snow-covered terrain in the southern Sierra Nevada.

In the spatial (geometric) domain, the scanning and sampling of the MSS defines a Cartesian coordinate system of lines and samples, by which individual pixels are referenced. Interactions between the scanner, the earth, and the spacecraft cause this coordinate system to be distorted both with respect to geographic coordinate systems, and between successive images of the same location. These distortions fall into two broad categories: systematic (which can be modelled using a priori information), and random (which must be modelled statistically). Mappings between MSS locations and other coordinate systems are usually accomplished by a combination of statistical error minimization (e.g. least squares) and systematic distortion models, applied to a set of control points with known coordinates in both systems (Van Wie and Stein, 1976). This procedure requires a method by which RNs may be assigned to non-integer MSS coordinates (resampling) should such coordinates correspond to a location of interest in the other coordinate system. High-order resampling schemes (such as "cubic convolution") are available which produce theoretically optimal interpolations of image RNs (Taber, 1973).

There are two major problems associated with the geometric preprocessing of MSS data for space radiance studies. First, the location of accurate image control points is a problem over many of the areas where satellite-derived space radiance data would be most useful. Areas lacking other means of surface exitance measurement are also often lacking in readily locatable cultural

features such as highway intersections and agricultural field boundaries. The previously cited example of the southern Sierra Nevada is a case in point. Second, high-order resampling of image RNs is not possible if the interpolation kernel includes threshold and/or saturated pixels, since interpolation by definition requires that the input values be bounded. This leaves zero-order or "nearest-neighbor" resampling as the only usable method under such circumstances. Unfortunately, nearest-neighbor resampling induces the greatest positional error of any resampling method (Nack, 1977).

Given the above background, the actual preprocessing procedure which we generally employ may now be described. A Landsat MSS CCT is received either with a standard radiometric calibration already applied, or with the necessary parameter values for the user to apply the calibration (Thomas, 1975). No further radiometric calibration is possible at the preprocessing level without corrupting the RN-to-radiance transformation. The data are left in RN format until completion of geometric preprocessing, in order to simplify the recognition of threshold or saturated pixels.

The object of the geometric preprocessing is to register the MSS data to the coordinate system of an area of interest extracted from NCIC Digital Terrain Tapes. The terrain tapes are an excellent database for radiation studies since information on elevation, slope, exposure, and horizon may be derived from them (Dozier and Outcalt, 1979). In areas of low relief, the necessary control points may be located on the MSS image and on maps,

whose latitude-longitude coordinates may be readily converted to indices in the terrain array. In areas of high relief, which due to remoteness are often associated with less accurate maps, the terrain tapes lend themselves to another method of identifying surface control points. It is possible to synthesize a shaded-relief map by assigning to each point on the terrain grid the cosine of the solar angle (measured from normal to the slope) at that point. If the sun position used to make the shaded relief map corresponds to that of the satellite overpass being registered, then the resulting image of cosines bears a strong resemblance to the satellite image. In particular, the illumination of prominent terrain features such as mountain peaks and ridge lines is the same, which permits these features to be used as control points even when they cannot be accurately located on available maps. Figure 1 illustrates a satellite image with systematic distortions removed, along with a shaded-relief map of the same general area.

The systematic distortions inherent in MSS data are compensated by removing the distortions from the control point MSS coordinates, and reintroducing them when MSS coordinates are selected for a terrain location. Several sources of systematic distortion have been identified in MSS imagery (Van Wie and Stein, 1976; Bernstein and Ferneyhough, 1975; Kirby and Steiner, 1978). Of these most are either insignificant over areas appreciably smaller than a full MSS frame (e.g. earth curvature, panoramic distortion), or can be treated as continuous and linear

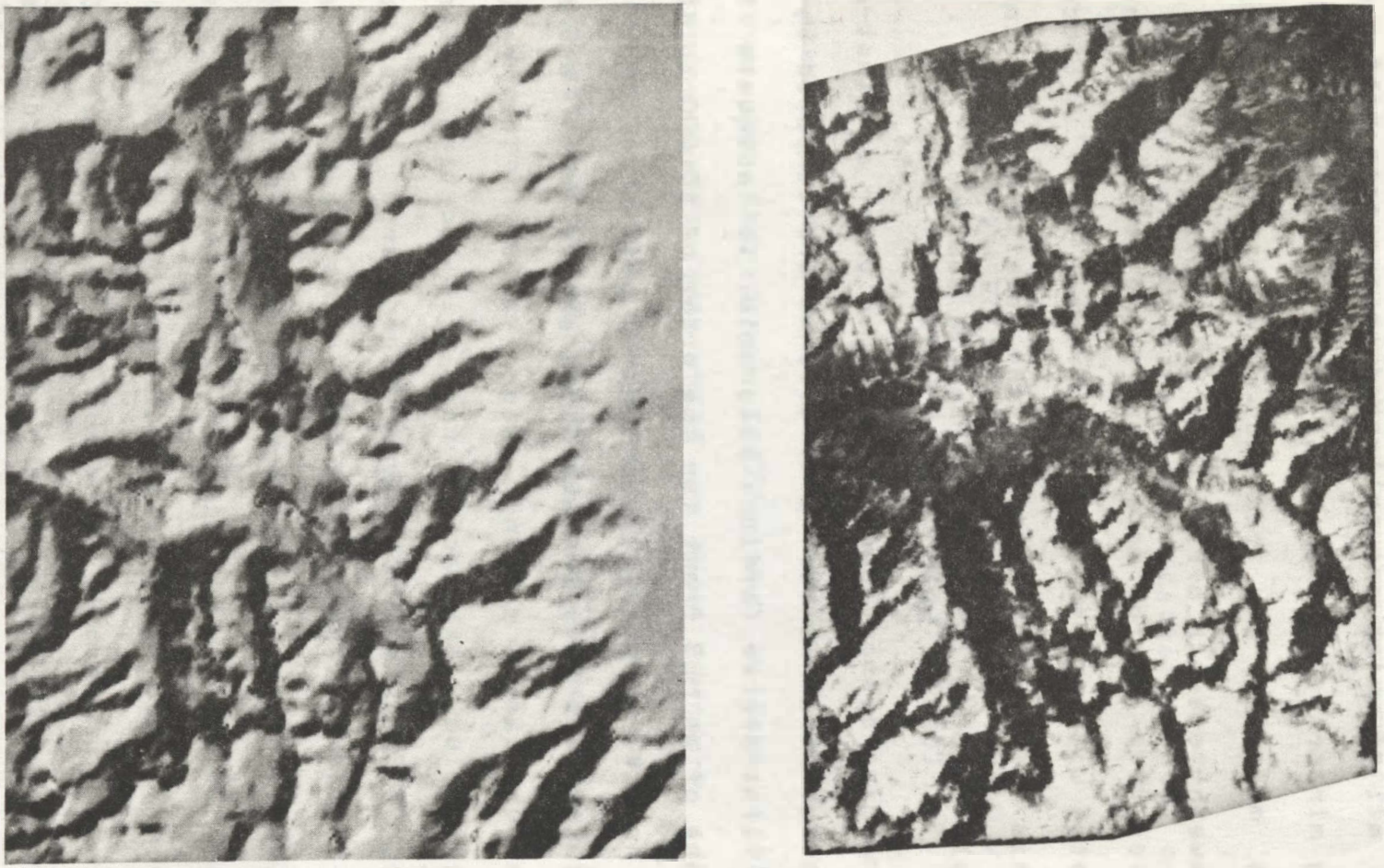

Figure 1.--See page 29.

over the entire image (e.g. scan skew, earth rotation, oversampling). A distortion which is neither continuous nor insiginificant results from the offset between scan swaths (a swath is 6 scan lines, all of which are collected on a single half-cycle of the scanning mirror). If the global skew resulting from earth rotation is modelled and removed as a continuous function, a "sawtooth" swath-to-swath offset will be apparent (Nack, 1977). This results from mirror motion and earth rotation in the time between samples within a swath (Holkenbrink, 1978). Since the bulk of this distortion is due to the precisely timed interval between sample acquisitions, it is readily removed.

The remaining distortions are subsumed under a first-degree bivariate polynomial, whose coefficients are computed by least squares. A first-degree (affine) polynomial is adequate for a small subscene of an MSS frame (on the order of 10,000 to 100,000 pixels) and has the advantage that control points which are inaccurately located will have anomalously high residuals, and may be removed from subsequent mapping (Wong, 1975). The resulting polynomial is evaluated at each terrain grid location, yielding a corresponding MSS image location. For large areas, direct evaluation of the polynomials at each point may be computationally prohibitive, necessitating some sort of coordinate interpolation scheme (Van Wie and Stein, 1976). This image location is "de-corrected" for the within-swath distortion, and an RN value is interpolated or simply fetched, as appropriate. Once a registered image is obtained, the RNs may be converted to L↑[λ]space by equation (3). Figure 2 is an example of a space radiance image which corresponds to known terrain coordinates.

The example is from the southern Sierra Nevada, and the corresponding mask of saturated pixels is also shown.

Path Radiance Algorithm

Total monochromatic radiation scattered out of the solar beam is:

$$E'[\lambda] = EO[\lambda]\, r^{-2} \{1 - \exp [-ma\, (\sigma A[\lambda] / (1+a/Re) + \sigma R[\lambda]\, P[z]/P[O])]\} \quad (4)$$

Tabulated data for the solar constant $EO[\lambda]$ are available from Makarova and Kharitinov (1972) and Willson (1978); Rayleigh scattering coefficients $\sigma R[\lambda]$ are from Penndorf (1957); atmospheric path length ma is calculated by Kasten's (1966) method. The aerosol scattering coefficient is parameterized by Angstrom's (1961, 1964) equation:

$$\sigma A[\lambda] = \beta[z]\, \lambda^{-\alpha} \quad (5)$$

A commonly accepted value for α is 1.3, with variations from 0.8 to 2.0 (Leckner, 1978). If λ is expressed in nm, β ranges from 0 to about 12,500.

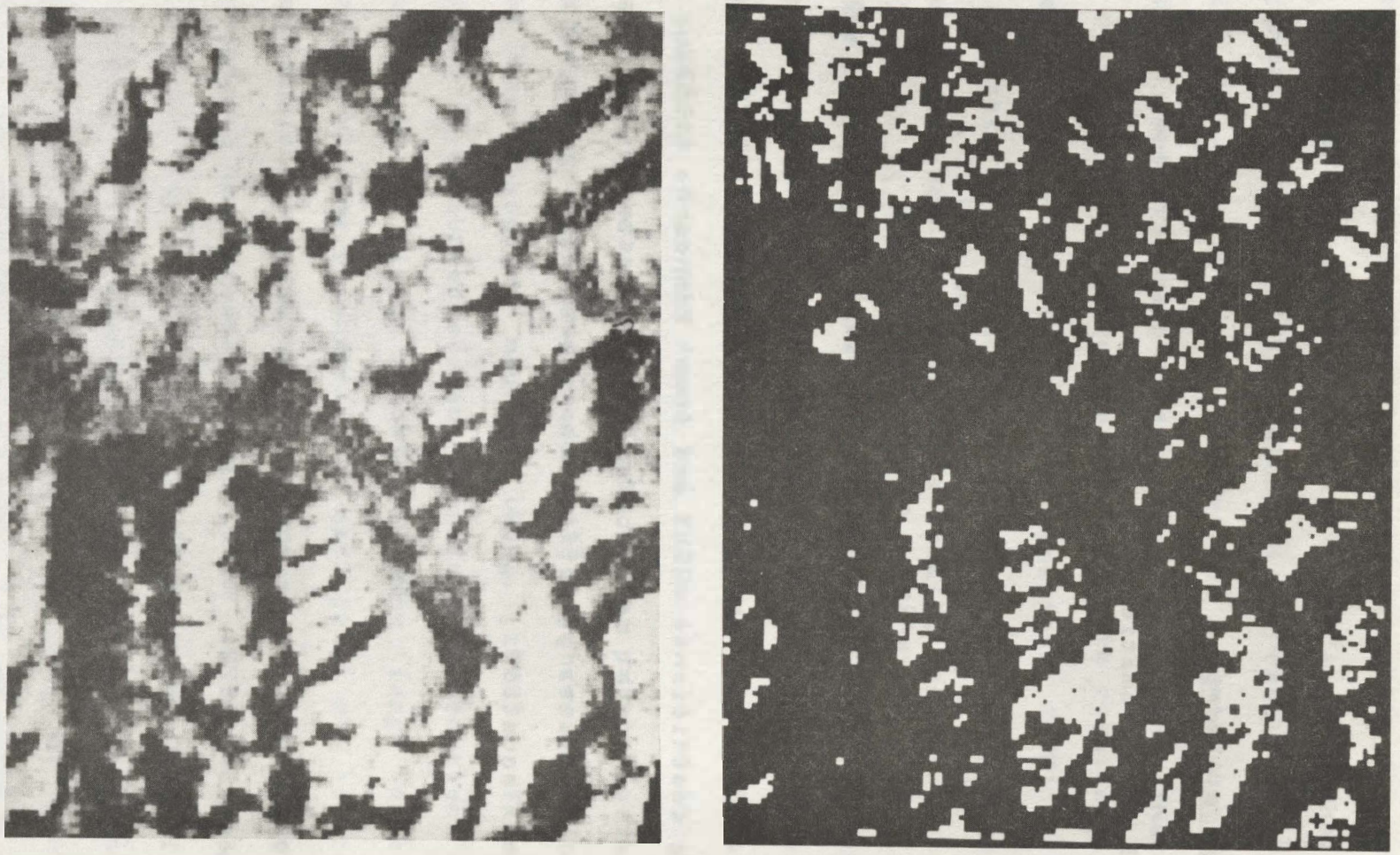

Figure 2.--See page 29.

Subsequent to scattering, the upwelling radiation is subject to absorption from ozone, water vapor, and aerosols. We assume that, on the average, the scattering takes place from level P[z]/2, where P[z] is surface pressure. This altitude (z2) can be found from the hydrostatic equation and the equation of state. The ozone (Kreuger and Minzner, 1974), precipitable water vapor (Yamamoto, 1949), and turbidity (Robinson, 1966) values for the atmosphere above altitude z2 are:

$$(O3)[z2\uparrow] = (O3)[0] - 2.5\times10^{-5}\ z2 \tag{6}$$

$$w[z2\uparrow] = w[0]\ \{1 - \exp\ [-4\times10^{-4}\ z2]\} \tag{7}$$

$$\beta[z2] = \beta[0]\ \exp\ [-5\times10^{-4}\ z2] \tag{8}$$

Hence the transmission function for the scattered radiation is:

$$\tau[\lambda] = \exp\ \{-[ko[\lambda]\ (O3)[z2\uparrow] + kw[\lambda]\ w[z2\uparrow] + \beta[z2]\ \lambda^{-\alpha}\ /\ (1 + 1/(a/Re))]\} \tag{9}$$

If a/Re = 0, the last term, for aerosol absorption, is omitted. Tabulated values for the absorption coefficients are available for ozone (ko[λ]) from Inn and Tanaka (1953) and Leighton (1961), and for water vapor (kw[λ]) from Gates (1960) and Gates and Harrop (1963).

Combining equations (4) and (9) leads to the path radiance:

$$L\uparrow[\lambda]path = 0.5 \cos^{4/3} Z \; E'[\lambda] \; \tau[\lambda] \; / \; \pi \qquad (10)$$

The first term (Robinson, 1966) accounts for the portion of the radiation scattered upward.

For a given solar zenith angle and atmospheric attenuation parameters, the path radiance is a function of surface elevation. Hence the integrals over the wavelength range of interest can be calculated for a range of elevations within the area of interest, and the path radiance may then be interpolated for each pixel, provided that each pixel's elevation is known. Sensitivity of path radiance to altitude and atmospheric aerosol content at two different solar zenith angles is shown in Figure 3. The highest Angstrom β value used is 3500, compared to our highest measured values (in the southern Sierra) of 4500. The lower β value used is 50; we have measured values below 10. The Figure demonstrates that path radiance is quite sensitive to altitude, solar angle, and atmospheric aerosols. Moreover, because of the dependence on altitude, it is likely that a single haze correction factor for an entire scene (e.g. Otterman and Fraser, 1976) will be incorrect for areas of rugged terrain.

Figure 4 illustrates dependence of path radiance on precipitable water vapor. Because water vapor absorption is important chiefly beyond 855 nm, the scales on both axes are different than in Figure 3.

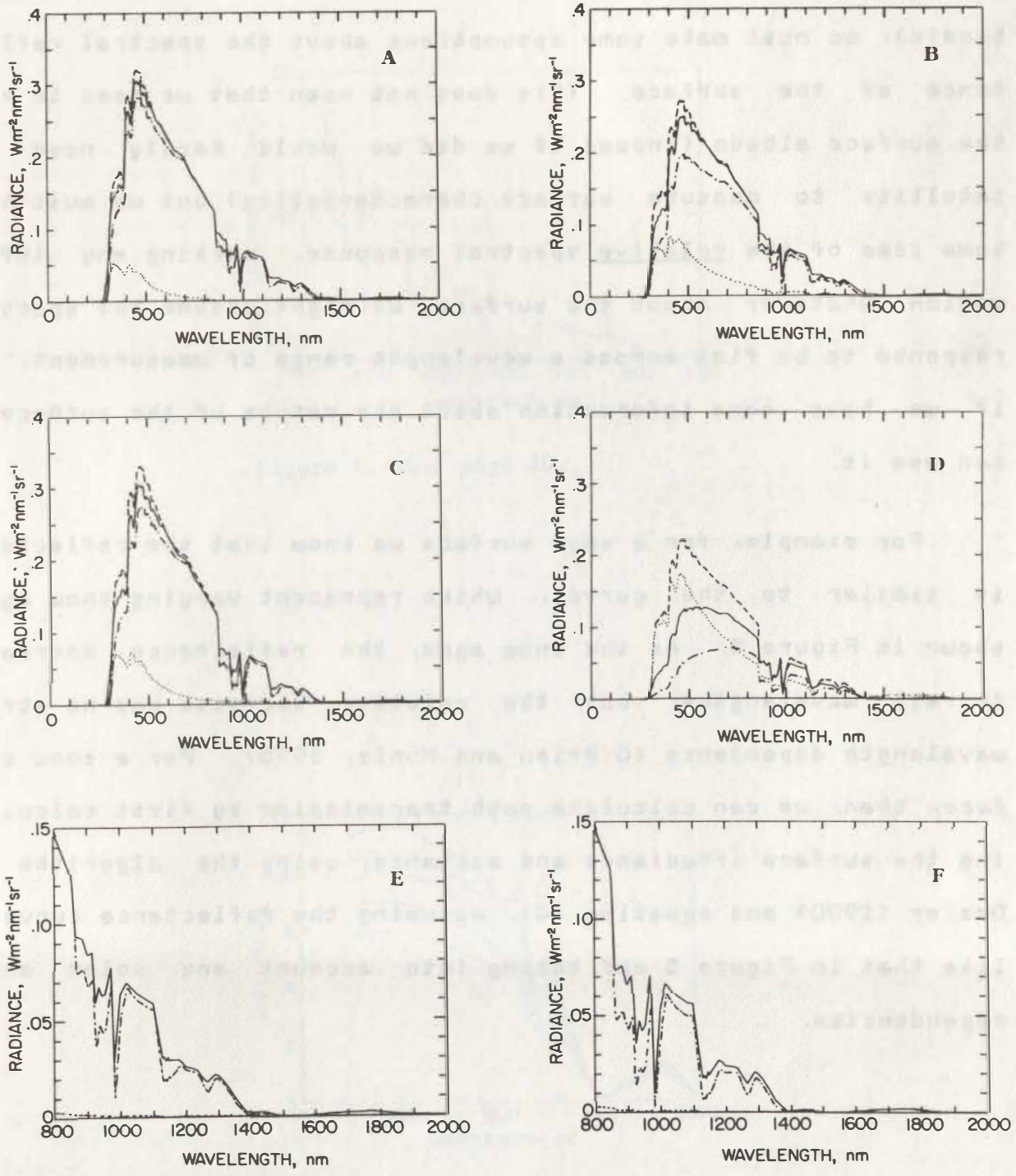

Figure 3.--See page 29.

Path Transmission Algorithm

In order to determine path transmission with a satellite radiometer measuring upwelling space radiance in broad wavelength band(s), we must make some assumptions about the spectral reflectance of the surface. This does not mean that we need to know the surface albedo (indeed if we did we would hardly need the satellite to measure surface characteristics) but we must have some idea of the relative spectral response. Lacking any information whatever about the surface, we might assume the spectral response to be flat across a wavelength range of measurement, but if we have some information about the nature of the surface we can use it.

For example, for a snow surface we know that the reflectance is similar to the curves, which represent varying snow ages, shown in Figure 5. As the snow ages, the reflectance decreases in all wavelengths, but the relative decrease has no strong wavelength dependence (O'Brien and Munis, 1975). For a snow surface, then, we can calculate path transmission by first calculating the surface irradiance and exitance, using the algorithm in Dozier (1980) and equation (4), assuming the reflectance curve is like that in Figure 5 and taking into account any solar angle dependencies.

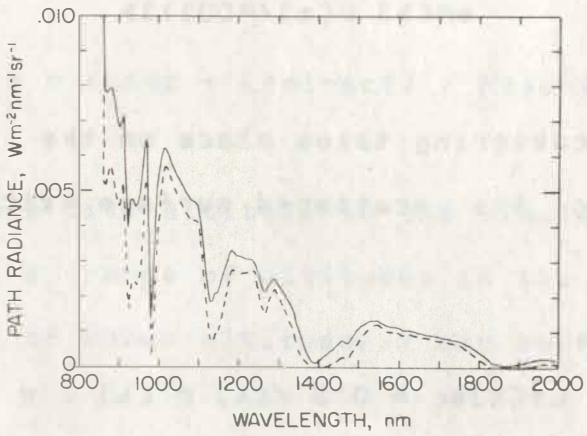

Figure 4.--See page 29.

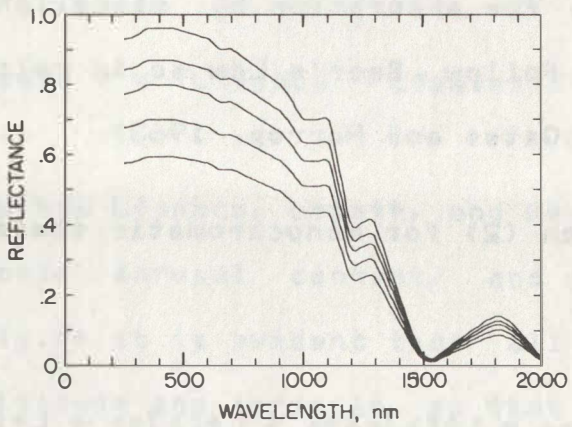

Figure 5.--See page 30.

As this radiation leaves the surface it is scattered and absorbed. The total amount scattered is:

$$M'[\lambda] = M[\lambda]surf \{1 - exp[-(\sigma A[\lambda] / (1+a/Re) + \sigma R[\lambda] P[z]/P[0])]\} \quad (11)$$

As before, this scattering takes place on the average from the level P[z]/2, so the scattered surface exitance which reaches space is:

$$L\uparrow[\lambda]sc = 0.5\ \tau[\lambda]\ M'[\lambda] / \pi \quad (12)$$

The surface exitance which is neither scattered nor absorbed before reaching space is:

$$L\uparrow[\lambda]direct = M[\lambda]surf\ \tau[\lambda]misc\ exp\ [-(ko[\lambda]\ (O3)[z\uparrow] + kw[\lambda]\ w[z\uparrow] + \sigma A[\lambda] + \sigma R[\lambda]\ P[z]/P[0])] / \pi \quad (13)$$

The $\tau[\lambda]misc$ term, for absorption by miscellaneous gases, does not necessarily follow Beer's Law so is calculated outside the exponential term (Gates and Harrop, 1963).

Hence equation (2) for monochromatic space radiance may be re-phrased:

$$L\uparrow[\lambda]space = L\uparrow[\lambda]path + L\uparrow[\lambda]sc + L\uparrow[\lambda]direct \quad (14)$$

This equation does not help us much, because our space measurements are of L↑space integrated over some $\Delta\lambda$. However, if we

have correctly specified the general form of $\rho'[\lambda]$ and $\rho[\lambda]$, then our calculations of $M[\lambda]surf$, $L\uparrow[\lambda]sc$, and $L\uparrow[\lambda]direct$ at least have the correct relative values. Hence if we integrate these over the desired $\Delta\lambda$ and drop the wavelength designation:

$$\tau = \pi \, (L\uparrow sc + L\uparrow direct) \, / \, M\uparrow surf \qquad (15)$$

The values of τ vary with altitude so the simulation has to be carried out for a range of altitudes in the area of interest. Then for any pixel of known altitude, τ can be found by interpolation.

Calculation of Surface Exitance

By the methods presented in the two previous sections, integrated values for $L\uparrow path$ and τ can be found for any wavelength range for any pixel of known elevation. By rearranging equation (1) the surface exitance is:

$$M\uparrow surf = \pi \, (L\uparrow space - L\uparrow path) \, / \, \tau \qquad (16)$$

In Figure 6 we show how $L\uparrow space$, $L\uparrow path$, and $M\uparrow surf/\pi$ vary with altitude, atmospheric aerosol content, and precipitable water vapor. From the Figure it is evident that all three variables are sensitive to altitude and aerosols, so that ad hoc techniques (such as band-ratioing) for estimating surface exitance will not work satisfactorily over a wide range of parameters. For the near-infrared wavelengths where water vapor absorption is the

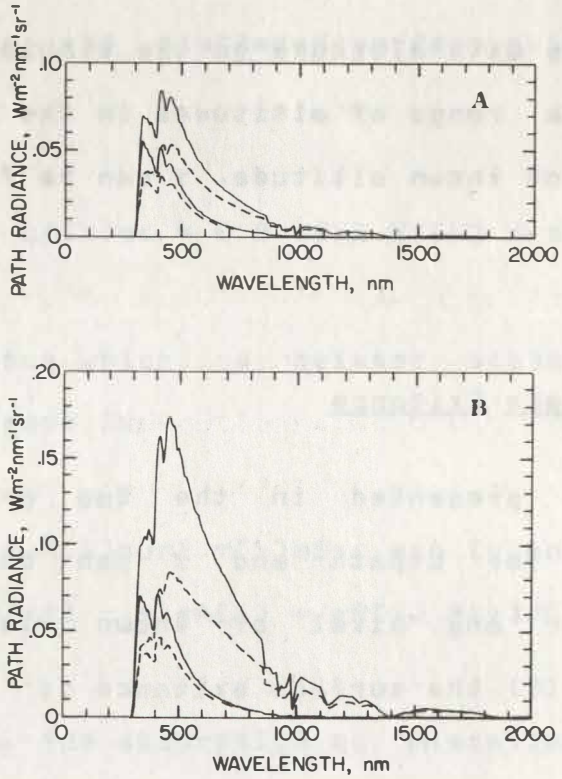

Figure 6.--See page 30.

major attenuation factor, corrections for path radiance can probably be ignored.

Conclusion

Path radiance and path transmission vary with the altitude of the surface, atmospheric aerosol and water vapor content, and the nature of the spectral reflectance of the surface. The variations involved are not trivial, and must be calculated explicitly if we are to derive surface exitance data from space-borne radiometers. Figure 7 shows, for the area in Figure 2, the difference between $L\uparrow_{space}$ and $M\uparrow_{surf}/\pi$ in MSS band 5, for 13 February 1977, when field measurements of solar radiation in two wavelength ranges (280-2800 nm and 700-2800 nm) indicated a β value of 1100 and 14 mm precipitable water vapor. For this band (and for band 6) none of the differences are negative. This indicates that the increased brightness of the image due to path radiance more than compensated for the atmospheric attenuation of the surface signal. This is not true, however, for similar analyses we made for MSS bands 4 and 7, where some of the differences were negative.

Figure 7.--See page 30.

REFERENCES

Angstrom, A., (1961) Techniques for determining the turbidity of the atmosphere, Tellus, 13: 214-223.

Angstrom, A., (1964) Parameters of atmospheric turbidity, Tellus, 16: 64-75.

Bernstein, R., and Ferneyhough, D.G. jr., (1975) Digital image processing, Photogramm. Engrg. Remote Sens., 41: 1465-1476.

Dozier, J., (1980) A clear-sky spectral solar radiation model for snow-covered mountainous terrain, Water Resour. Res., (to appear).

Dozier, J., and Outcalt, S.I., (1979) An approach toward energy balance simulation over rugged terrain, Geog. Analysis, 11: 65-85.

Gates, D.M., (1960) Near infrared atmospheric transmission to solar radiation, J. Opt. Soc. Amer., 50: 1299-1304.

Gates, D.M., and Harrop, W.J., (1963) Infrared transmission of the atmosphere to solar radiation, Appl. Optics, 2: 887-898.

Holkenbrink, P.F., (1978) Manual on characteristics of Landsat computer-compatible tapes produced by the EROS Data Center digital image processing system, User Services Section, U.S. Geological Survey, EROS Data Center, Sioux Falls, SD.

Inn, E.C.Y., and Tanaka, Y., (1953) Absorption coefficient of ozone in the ultraviolet and visible regions, J. Opt. Soc. Amer., 43: 870-873.

Kasten, F., (1966) A new table and approximation formula for the relative optical air mass, Arch. Meteorol. Geophys. Bioklim., ser. B, 14: 206-223.

Kirby, M., and Steiner, D., (1978) The appropriateness of the affine transformation in the solution of the geometric base problem in Landsat data, Can. J. Remote Sens., 4: 32-43.

Kreuger, A.J., and Minzner, R.A., (1974) A mid-latitude ozone model for the U.S. standard atmosphere, NASA Goddard Space Flight Center, report no. X-912-74-291, 17 pp.

Landgrebe, D.A., et al., (1974) A study of the utilization of ERTS-1 data from the Wabash River Basin, final report contract no. NAS5-21773, NASA Goddard Space Flight Center, 337 pp.

Leckner, B., (1978) The spectral distribution of solar radiation at the earth's surface -- elements of a model, Solar Energy, 20: 143-150.

Leighton, P.A., (1961) Photochemistry of Air Pollution, Academic Press, New York, pp. 6-103.

Makarova, Ye.A., and Kharitinov, A.V., (1972) Distribution of energy in the solar spectrum and the solar constant, NASA TT F-803, 245 pp.

Nack, M.L., (1977) Rectification and registration of digital images and the effect of cloud detection, in 1977 Machine Processing of Remotely Sensed Data Symposium, LARS, Purdue University, West Lafayette, IN, pp. 12-23.

NASA (1976) Landsat data users handbook, NASA Goddard Space Flight Center, document no. 76SDS4258,

O'Brien, H.W., and Munis, R.H., (1975) Red and near-infrared spectral reflectance of snow, in Workshop on Operational Applications of Satellite Snowcover Observations, (Rango, A., Ed.), NASA SP-391, pp. 319-334.

Otterman, J., and Fraser, R.S., (1976) Earth-atmosphere system and surface reflectivities in arid regions from Landsat MSS data, Remote Sens. Environ., 5: 247-266.

Penndorf, R., (1957) Tables of the refractive index for standard air and the Rayleigh scattering coefficient for the spectral region between 0.2 and 20.0 microns and their application to atmospheric optics, J. Opt. Soc. Amer., 47: 176-182.

Potter, J.F., (1977) The correction of Landsat data for the effects of haze, sun angle, and background reflectance, in Symposium on Machine Processing of Remotely Sensed Data, LARS, Purdue University, West Lafayette, IN, pp. 24-31.

Robinson, N., Ed., (1966) Solar Radiation, Elsevier, Amsterdam, pp. 29-160.

Taber, J.E., (1973) Evaluation of digitally corrected ERTS images, Third ERTS-1 Symposium, vol. 1-B, pp. 1837-1844.

Thomas, V.L., (1975) Generation and physical characteristics of Landsat 1 and 2 MSS computer compatible tapes, NASA Goddard Space Flight Center, report no. X-563-75-233, 70 pp.

Van Wie, P., and Stein, M., (1976) A Landsat digital image rectification system, in Symposium on Machine Processing of Remotely Sensed Data, LARS, Purdue University, West Lafayette, IN, pp. 4A18-4A26.

Willson, R.C., (1978) Accurate solar 'constant' determinations by cavity pyrheliometers, J. Geophys. Res., 83: 4003-4007.

Wong, K.W., (1975) Geometric and cartographic accuracy of ERTS-1 imagery, Photogramm. Engrg. Remote Sens., 41: 621-635.

Yamamoto, G., (1949) Average vertical distribution of water vapour in the atmosphere, Tohuku Univ. Sci. Rep., ser. 5, 1: 76-79.

FIGURE CAPTIONS

1. Shaded relief map (left) and Landsat image with systematic distortions removed (right). The area is approximately a 15-minute quadrangle in the Kearsarge Pass - Bullfrog Lake region of the southern Sierra Nevada, in the Kings River drainage, South Fork.

2. The Landsat image from Figure 1 corrected to terrain, so that each pixel corresponds to a known coordinate on a digital terrain tape. On the right is a mask of saturated pixels. Unsaturated radiances in the image range from 0 to 17.5 W m^{-2} sr^{-1} (integrated from 600 to 700 nm).

3. Sensitivity of path radiance to altitude, solar angle, and atmospheric aerosols. (A) is for 3000 m elevation. (B), whose ordinate scale is the same, is for sea level. In each graph the solid lines represent May 30 at latitude 36.5 deg N; the dashed lines represent December 21 at the same latitude. In both cases the time of day is that corresponding to the Landsat overpass, about 9:37 a.m. For each date the upper curve represents path radiance for $\beta = 3500$; the lower curve represents path radiance for $\beta = 50$. Both the magnitude and the spectral distribution of path radiance are sensitive to altitude, solar angle, and aerosols.

4. Sensitivity of path radiance to precipitable water vapor. The analysis is for May 30 at the location and time of day corresponding to Figure 3. The upper (solid) curve is for $w = 10$ mm; the lower curve (dashed) is for $w = 40$ mm. Because

water vapor absorbs some of the light which has been scattered upward, increased water vapor will decrease the path radiance, in contrast to the situation shown in Figure 3.

5. Snow reflectance vs wavelength. The top curve represents new snow. The lower curves represent the degradation in reflectance that occurs as the snow ages.

6. Sensitivity of surface upwelling radiance $M\uparrow surf/\pi$ (solid line), space radiance $L\uparrow space$ (dashed line), path radiance $L\uparrow path$ (dotted line), and the transmitted signal $L\uparrow space - L\uparrow path$ (dot-dashed line), to altitude, atmospheric aerosols, and precipitable water vapor. (A) is for 3000 m elevation, 10 mm water vapor, and $\beta = 50$. (B) is like (A), except that $\beta = 3500$. (C) and (D) are for the same parameters as in (A) and (B) at sea level. (E) and (F) show sensitivity to water vapor at 3000 m elevation; (E) is at $w = 10$ mm, while (F) is at $w = 40$ mm. All of these simulations are for a horizontal surface.

7. The difference between upwelling radiance in space and at the surface for MSS band 5, derived from the image in Figure 2. Values range from 0 to 1.54 W m sr (but almost all of the 0 values are for saturated pixels). For this overpass, field measurements of solar radiation indicated a β value of 1100, with 14 mm precipitable water vapor.

Remote Sensing of Snow Surface Albedo

James Frew

Department of Geography
University of California
Santa Barbara, California

ABSTRACT

Surface energy-balance simulation models require values for surface albedo in order to calculate net solar radiation. When such models are to be evaluated over an extensive area of high relief, as in the case of alpine snowmelt regions, accurate on-site measurement of albedo at adequate temporal and spatial resolutions may not be possible. Existing databases and simulation methods offer a solution to this problem, if properly integrated. Digital terrain data and numerical atmospheric models are used to derive point spectral irradiances. Spaceborne radiance measurements, combined with this information, are used to compute a surface albedo for any given terrain location. The method presented for accomplishing this integration and calibration accounts for geometric distortions between the image and terrain grids, and for atmospheric effects on the space radiance data.

TABLE OF CONTENTS

LIST OF SYMBOLS

α	:	global surface reflectance (albedo)
β	:	parameter in Angstrom turbidity function
Δ	:	change in
λ	:	wavelength
ρ	:	diffuse reflectance of beam irradiance
ρ'	:	diffuse reflectance of diffuse irradiance
τ	:	atmospheric transmissivity
A	:	local azimuth (orientation), measured clockwise from south
A'	:	solar azimuth, as above
AD	:	net advective (i.e., by mass movement) transfer
ar	:	angle of refraction
[band]	:	"per MSS band"
C	:	function relating $\rho[0]/\rho'$ to z
E	:	global shortwave irradiance
Ed	:	diffuse irradiance
Es	:	beam irradiance
f	:	beam (specular, Fresnel) reflectance of beam irradiance
G	:	net snow-soil heat transfer
g	:	empirical function relating $\rho[Z]$ to $\rho[0]$
H	:	net snow-atmosphere sensible heat transfer
ir	:	index of refraction
K	:	snow "effective age" parameter
k	:	parameter in "g" function

km	:	kilometer
L↑	:	upwelling radiance
Ldirect	:	non-scattered radiance
LE	:	net snow-atmosphere latent heat transfer
Lsat	:	saturation radiance
Lsc	:	scattered radiance
Lthresh	:	threshold radiance
M	:	global shortwave exitance
Msurf	:	surface exitance
m	:	meter
mr	:	milliradian
nm	:	nanometer
Q	:	heat storage
R	:	net radiation
Ri	:	net longwave (terrestrial and atmospheric) radiation
Rs	:	net shortwave (solar) radiation
S	:	local slope angle, from horizontal
sr	:	steradian (solid angle)
Vf	:	sky view factor
Vt	:	terrain view factor
W	:	watt
Z	:	solar zenith angle, with respect to true vertical
Z'	:	solar zenith angle, with respect to local surface normal
z	:	elevation

1. Objective

The objective of this investigation has been the development of a procedure for deriving an estimate of the spectral albedo of an extensive alpine snow cover from satellite spectral radiance measurements. The procedure is demonstrated with Landsat digital imagery of the southern Sierra Nevada, and the resultant spectral albedo measurements are adequate for input to an areally extensive energy-balance snowmelt model.

2. Introduction

2.1. Significance of Albedo in Energy-Balance Modeling

Energy-balance snowmelt modeling is an attempt to compute the water released from a melting snowpack by measurement and/or simulation of all energy exchanges involving the snowpack. The sum of these energy transfer processes is expressed as the energy-balance equation (after Sellers, 1965; and Anderson, 1976):

$$R + G + H + LE + AD = \Delta Q \qquad (1)$$

Flows of energy into the pack are positive; flows out

(energy losses) are negative. Once the pack is isothermal, a net positive energy flow results in melt.

The net radiation exchange term may be broken down into net shortwave (solar) and net longwave (terrestrial and atmospheric) components:

$$R = Rs + Ri \qquad (2)$$

The net shortwave radiation is the difference between the total incident solar radiation (irradiance) and the total reflected solar radiation (exitance):

$$Rs = E - M \qquad (3)$$

The shortwave exitance of a surface under a given irradiance is a function of the total reflectance or albedo of the surface:

$$M = \alpha E \qquad (4)$$

Net shortwave radiation may thus be computed if values for any two of the three parameters albedo, exitance, and irradiance are available.

2.2. The Need for an Albedo Model

To date, energy-balance snowmelt models have been demonstrated only for very small areas for which on-site irradiance and exitance measurements at a single fixed location have been adequate (e.g. Anderson, 1976). In such cases, net shortwave radiation may be computed directly from equation (3). For an areally extensive energy-balance snowmelt model, such as is currently being developed for several drainage basins in the southern Sierra Nevada (Dozier et al, 1978b), direct measurement of irradiance and/or exitance (and therefore albedo) is not practical. The extreme spatial variation in terrain parameters affecting radiation geometry (slope, aspect, local horizons, sky and terrain view factors, etc.) would require an enormously expensive instrument network, over an area with at best limited winter accessibility. The net radiation at given points within the study area must thus be derived by indirect means.

Spectral irradiance over a topographic surface may be estimated from digital terrain data, astronomical parameters, and a limited set of field measurements which are used to calibrate an atmospheric radiance and

transmission model (Dozier, 1979). These measurements are available at two continuously recording sites in the southern Sierra snowmelt study area; therefore, values for spectral irradiance may be estimated for any location given date and time. To compute net radiation, a similar procedure is needed for either exitance or albedo.

Spaceborne shortwave radiometers, especially imaging scanners such as the Landsat multispectral scanner (MSS) (NASA, 1976), yield measurements of surface exitance convolved with the path radiance and transmission functions of the intervening atmosphere, and modulated by the characteristics of the instrument. Given field data from which these atmospheric effects may be modelled, it is possible to derive the aggregate surface exitance of the locations corresponding to the radiometer's instantaneous field of view (IFOV), at the time of the satellite overpass (Dozier and Frew, 1980). Such surface exitance measurements are valid only for the time of acquisition. This usually occurs too infrequently (e.g., every 9 days for a pair of Landsat satellites), or at too coarse a spatial resolution (e.g., 1 km for the NOAA/TIROS satellites), to be directly useful for net radiation calculations, which are typically made at intervals of at most

one day (Anderson, 1976). In addition, spaceborne radiometers typically measure only a limited portion of the shortwave spectrum (e.g., 500 - 1100 nm for the Landsat MSS).

From simulated irradiance and satellite-derived exitance, it is possible to compute a grid of albedos over the study area. This calculation would seem to be likewise subject to the spectral and spatiotemporal constraints imposed by the spaceborne radiometer. However, known reflectance characteristics of snow, which are reviewed in section 3, allow us to extrapolate spectrally from albedo measurements which are otherwise unacceptably constrained in this dimension. Once this spectral signature has been obtained, it should be possible to update it at low spatial resolutions during the interval between high-resolution satellite overpasses. For this reason an albedo model has been developed to complete the net radiation input to the snow energy balance model.

2.3. Overview of the Model

The snow surface albedo model which this paper develops may be summarized as follows:

- Create terrain data for the selected study area. The current model uses a regular grid of points at 100 m spacing. At each point, compute values for terrain factors which are known to influence solar radiation.

- Obtain satellite radiometry of the study area from a suitable sensor (e.g., Landsat MSS data). Register these data to the terrain grid, such that each grid point may be assigned a space radiance value. Using minimal coincident field radiometry to calibrate the necessary atmospheric models (see section 4.4.1), convert space radiance to surface exitance at each point.

- Estimate shortwave irradiance at each grid point, using the same atmospheric and astronomic parameters as in the exitance derivation.

- Derive the components of surface albedo at each grid point. In addition, compute an "effective age" for the snow cover at each point, which can be used for spectral albedo extension.

The following data requirements are imposed by this procedure:

- an elevation for each grid point in the study area.

- satellite shortwave radiometry of the study area, at appropriate spectral, spatial, temporal, and radiometric resolutions.

- field shortwave radiation measurements as required to calibrate atmospheric radiance and transmission models.

- specifications of the characteristics of snow albedo.

3. Background

3.1. Characteristics of Snow Albedo

The model developed herein is to a large degree dependent on the ability to specify in advance certain reflectance characteristics of a snow-covered surface. The following is a brief review of existing literature on this subject.

3.1.1. Temporal Characteristics

The albedo of a snowpack has long been observed to decrease with age. Global albedo measurements (i.e., integrated over all directions and wavelengths) made by the U.S. Army Corps of Engineers (1956) at a Sierra Nevada site over a period of eight years, yielded the albedo decay or "aging" curves shown in figure (1). The shapes of these curves indicate the presence of two distinct components in the albedo decay process:

- The larger initial rate of albedo decay for an ablating versus an accumulating snowpack indicates a strong inverse relation between snow albedo and melt-related snowpack metamorphism (e.g., congealing of individual grains by melting-refreezing; presence of liquid water in the snowpack).

- The similar shapes of the two curves indicate a component of albedo decay which is independent of melt; namely, gravitational compaction and consequent

mechanical abrasion and sintering of the individual flakes. (Perla and Martinelli, 1975).

Petzold (1977) demonstrated that both curves are basically exponential decay functions of the form:

$$\alpha[i] = \alpha[i-1](1 - 10^{**}(a - bi)) \qquad (5)$$

where i is the age of the snowpack in days. Values for a and b which reproduce the curves in figure (1) are:

	a	b
accumulation	.78	.069
ablation	1.05	.07

Of course, these values are site-specific and cannot be used in a predictive fashion. The usefulness of equation (5) lies in its description of the general form of albedo decay over time.

Theoretical models of snow albedo indicate that the primary parameter governing changes in reflectance at a given wavelength is the change in size of the individual snow grains as the pack metamorphoses. Dunkle and Bevans (1956), Giddings and LaChapelle (1961), and Bergen (1975) modelled snow albedo based on the assumption that snow is a diffusing medium. In these models, light entering the

snowpack proceeds in a random-walk fashion governed by its interactions with individual snow grains. As grain size increases, so does the probability that an incident light beam will be either transmitted or scattered forward. Figure (2) presents plots of snow spectral albedo from the Dunkle-Bevans model, showing the effect of varying the grain size parameter.

Unfortunately, no simple analytic relationship has been developed between snowpack age and snow grain size; indeed, under some circumstances snow grain size may actually decrease over time (Perla and Martinelli, 1975). For shallow snowpacks, melt-induced metamorphism will be much more rapid as radiation penetrates to the ground surface, is absorbed, and is then conducted and/or re-radiated back into the pack, accelerating the melt rate (USACE, 1956; O'Neill and Gray, 1973). Also, an increase in snow density by gravitational compaction can have an effect on albedo similar to an increase in grain size (Bergen, 1975). It is thus inappropriate to extrapolate the decay of snow albedo solely by means of an empirical function of elapsed time. In the remainder of this paper, the "aging" of a snowpack will refer to the collection of processes acting to reduce the snow surface al-

bedo. Similarly, the "age" of a snowpack will be a dimensionless index of the status of these albedo-reducing processes, rather than an actual elapsed time.

3.1.2. Spectral Characteristics

The most comprehensive spectral measurements of snow reflectance available to date are those by O'Brien and Munis (1975). The measurements were made in a cold laboratory, using barium sulfate as a reflectance standard. Their "typical" spectral reflectance curve for new snow is shown in figure (3). The most striking feature of this curve is the rapid decrease in spectral reflectance in the infrared wavelengths (> 700 nm), as opposed to the familiar, uniformly high reflectance in the visible portion of the spectrum. As O'Brien and Munis note, this can be almost entirely ascribed to the variation in the spectral absorption coefficient of pure ice (see figure (4); data from Irvine and Pollack, 1968; Hobbs, 1974).

Theoretical albedo models whose snow transmissivity functions are driven by these spectral absorption data (Dunkle and Bevans, 1956; Giddings and LaChapelle, 1961; Choudhury and Chang, 1979) yield curves that quite closely agree with the O'Brien and Munis "reference" curve,

for snow grain sizes which are reasonable for new snow (Choudhury and Chang, 1979). Moreover, by increasing the grain size, the albedo is decreased at all wavelengths in a manner similar to that observed by O'Brien and Munis for naturally aged snow. It is important to note that in both the models and the measurements, the ratio of the spectral reflectances for any two wavelengths remains constant, while the absolute reflectance decreases at all wavelengths. In fact, when the O'Brien and Munis curve is multiplied by dimensionless, constant "aging factors", a family of new curves is generated (see figure (5)) which are quite similar to those generated by the theory-based models when their grain-size parameters are varied (see figure (2)).

3.1.3. Diffuse and Specular Components

Although for most purposes snow is assumed to be a diffuse (Lambertian) reflector, in reality it is well known that there is a significant specular component in snow reflectance. Measurements by Hubley (1955), the Corps of Engineers (1956), and Dirmhirn and Eaton (1975), using global pyranometers, all show a pronounced increase in albedo at large (typically > 60 deg) solar zenith an-

gles. If the specular component is assumed to behave according to Fresnel's law (Feynman et al, 1963), then its relative insignificance at lesser zenith angles is understandable. Figure (6) is a graph of the Fresnel reflectance of pure ice as a function of the angle of incidence of the beam irradiance.

A model of directional reflectance from snow was developed by Middleton and Mungall (1952) from extensive in situ measurements with a portable goniophotometer. The directional component of the reflectance was adequately explained by a Fresnel model. Their observation that for beam irradiance, the angle of reflection tended to be slightly larger than the angle of refraction, was explained by considering the snow surface to consist of myriad small, randomly oriented reflecting surfaces. The rapid rise in the Fresnel reflectance curve at large angles of incidence thus disproportionately favors those surfaces oriented nearer to parallel with the incoming beam.

Snow reflectance of beam irradiance actually consists of two components, the direct, Fresnel component (f) and the diffuse component (ρ). For normal incidence

(Z = 0), f[Z] is negligible. and reflectance measurements may be assumed to be yielding ρ[0]. For non-zero values of Z, the following relationship between f[Z] and ρ[Z] is noted (Paltridge and Platt, 1976):

$$\rho[Z] + f[Z] = \rho[0] + (1 - \rho[0])g[Z] \qquad (6)$$

where:

$$g[Z] = \exp[-k(90 - Z)];\ Z \text{ expressed in degrees} \qquad (7)$$

For most natural substances, including snow, k has a value of about 0.1.

Over a natural snow surface, there will be both direct and diffuse irradiance, and therefore a diffuse reflectance of diffuse irradiance (ρ′) in addition to the components ρ and f. The model presented in this paper includes a method for separating ρ and ρ′.

3.2. Digital Terrain Data

The geometric radiation information required for point calculations of surface net radiation, may be derived entirely from the regional elevation function (ignoring, for the time being, the effects of vegetative cover). A discrete approximation to this function, in

the form of a grid of elevation values at regular intervals of latitude and longitude, has been compiled for the entire U.S. by the National Cartographic Information Center, and is distributed as "Digital Terrain Tapes" (DTTs) in files of 1-degree-square geodetic quadrangles.

The DTTs were compiled by digitization of 1:250,000 scale topographic maps, at intervals of .01 inch, for a nominal surface x-y resolution of 63.5 m (in fact the grids are aligned to geodetic parallels and meridians, yielding a systematically variable grid spacing). This resolution appears to exceed the inherent resolution of such a small-scale map, and in fact both positional and elevation errors are frequently found for sharply defined features such as mountain peaks (Marks and Dozier, 1979). In addition, it has been noted that adjacent DTT grid columns are frequently misaligned, although sufficient ancillary data are usually provided to correct this problem. Offsetting these resolution problems, however, are the DTTs' ubiquity and reasonable price. In the absence of special local data, the DTTs are the logical choice for developing the terrain information required by the albedo model.

3.3. Characteristics of Landsat MSS Data

Landsat MSS data were selected as the remote sensing component of this investigation because the radiometric, spatial, spectral, and temporal resolutions of the MSS system represent the best compromise of the currently available spaceborne sensors. In this subchapter, the relevant characteristics of MSS data in each of these domains are evaluated. Readers unfamiliar with the MSS system are directed to NASA (1976) for an overview, since the following discussions assume a general familiarity with the instrument.

3.3.1. Radiometric Characteristics

The parameters governing the radiometric resolution of the MSS are dynamic range, precision, and accuracy. Dynamic range refers to the range of input radiance levels which the MSS accepts between its threshold (the highest intensity which cannot be distinguished from zero) and saturation (the lowest intensity which causes a sensor overload) levels. The precision is the smallest change in radiance which the sensor can resolve. Accuracy describes how well the radiance reported by the sensor corresponds to the actual target radiance.

The dynamic range of the MSS is inadequate for snow cover observations. Investigators have reported as many as 75 percent of the pixels in MSS band 5, and up to 25 percent in band 7, to be saturated in MSS imagery acquired over a snow-covered surface (Wiesnet et al, 1974). The disparity in saturation between bands is predictable if one considers the spectral reflectance characteristics of snow (see figure (3)).

The precision of the MSS data, for all bands and all Landsats, is better than 1 W m**-2 sr**-1, which is more than adequate for energy balance studies. Conversion of MSS digital radiance numbers (RNs) to target spectral radiance (L↑space[band]), is accomplished using the threshold and saturation radiances from table (1) in the following linear transform:

$$L\uparrow space[band] = (RN[band] / RNmax[band]) * (Lsat[band] - Lthresh[band]) + Lthresh[band] \quad (8)$$

The accuracy of the MSS data cannot be readily determined. The specifications call for an absolute accuracy of ±5 percent. Prelaunch tests indicate a potential accuracy of ±1.5 to 6 percent, varying by band (Ad

Hoc Advanced Imagers and Scanners Working Group, 1973). In-flight detector calibration is effected by exposing each individual detector to an on-board standard lamp, and statistically deriving the coefficients of a two-parameter linear correction from the observed variation in detector response (NASA, 1976). This correction has not been entirely successful in removing interdetector response variations (visually apparent as "striping" in MSS imagery); as a result, NASA has modified the linear correction described above to include additional multiplicative and additive correction factors derived from cumulative analysis of the existing corpus of MSS data (NASA, 1977).

In spite of these efforts, interdetector response variations persist in MSS data. It thus appears that the present combination of internal and historical calibration is not entirely adequate.

3.3.2. Spatial Characteristics

The spatial characteristics of MSS data that most concern this investigation are pixel resolution and image geometry. Pixel resolution refers to the earth surface area corresponding to a single MSS pixel, while image

geometry refers to inter-pixel positional relationships.

Pixel resolution or "size" is determined primarily by the IFOV of the MSS and the altitude of the satellite platform. The nominal values of these parameters (0.086 mr and 919 km, respectively) yield a pixel size of 79 m (on a side, since the detector aperture is square) at the nadir. Variations in this value of at most ± 2 m are caused by changes in satellite altitude, and by panoramic effects towards the ends of the scan lines. This resolution is quite compatible with the nominal grid spacing of the DTTs. In fact, Landsat MSS data are the only readily available spaceborne radiometric measurements possessing resolution to this order of magnitude.

Although MSS data are logically organized as a grid of pixels forming an image, the actual earth surface positional relationships of these pixels are quite complex. The factors which produce these distortions (in the sense of the departure of the image from an orthonormal grid of equally spaced lines and samples) are both systematic (i.e., predictable) and random. The most prominent systematic distortions, and their approximate magnitudes, are (based on data from NASA, 1976):

- earth rotation: The rotation of the earth beneath the MSS during the scan retrace causes each successive scan swath (a group of six adjacent scan lines acquired on the same scan half-cycle) to be displaced to the east of the previous swath. The resulting effect is a horizontal skew, variable with latitude, whose maximum is about 35 m per swath at the equator.

- scan skew: The forward motion of the satellite during a single scan results in a fairly constant cross-scan skew of about 240 m from one end of a line to the other.

- sampling delay: The six detectors per band which make up a scan swath are sampled sequentially. Scan mirror motion during the interval between samples causes a fixed displacement of about 4m between corresponding samples in adjacent lines in the same swath.

- oversampling: The electronic sampling rate of the MSS yields 1.41 samples per IFOV. This results in an along-scan pixel overlap with a nominal sample spacing of 56 m, while maintaining the nominal 79 m line spacing.

- panorama and earth curvature: The object plane of the MSS is essentially a cylinder whose axis is the spacecraft orbit and whose radius is the spacecraft altitude. The projection of the object plane onto the surface of the earth causes the earth distance between samples to increase as a function of the tangent of the scan nadir angle, yielding a maximum positional error of about 400 m at either end of a scan line (Kirby and Steiner, 1978; see figure (7)).

- scan nonlinearity: The acceleration/deceleration of the MSS scan mirror during an active (scanning) half-cycle introduces a sinusoidal displacement of samples along the scan line. The maxima of this effect occur at about one-quarter and three-quarters of the way through the scan, with magnitudes of about +400 m and -400 m, respectively (Thomas, 1975).

The above distortion sources do not account for all of the positional error in the MSS data. It was originally suggested by NASA that spacecraft attitude changes (yaw, pitch, roll) could introduce up to 674 m of essentially random positional error, owing to the poor resolution of the on-board attitude sensors (NASA, 1971). Although subsequent investigations suggest that these errors may in fact be much less (Wong, 1975), they must still be accounted for. Given that geometric correction to this level of accuracy is almost always for the purpose of registering the MSS data to an existing geographic database, the most common procedure for removing random distortions is a polynomial transform whose coefficients are derived by analyzing the displacement between the coordinates of control points which are identifiable in both the MSS data and in the target database. The combination of systematic and random distortion models can generally achieve geometric registration accuracies to within 1 pixel (Bernstein and Ferneyhough, 1975).

Given mathematical models of the above distortion processes, it is then possible to adjust the line and sample coordinates of the individual pixels so that they

refer to a coordinate space in which the distortions are not present. In practice, this procedure is usually applied in reverse; that is, an "empty" image is created whose regular grid is assumed to be free of any geometric distortions, and inverse distortion models are evaluated at each "empty" location to find the coordinates of the original image pixel to place there (Van Wie and Stein, 1976; Bernstein and Ferneyhough, 1975). The original image coordinates so derived are unlikely to be integral; therefore, an interpolation or resampling rule is required to compute an RN value to assign to the corrected grid. The simplest of these, requiring no interpolation at all, is nearest-neighbor assignment (i.e., the original image coordinates are rounded to the nearest integral value). The most effective tradeoff between radiometric accuracy and computational speed appears to be a third-order, "cubic convolution" interpolator, which computes a new RN from a 4x4 kernel in the original image (Taber, 1973).

3.3.3. Spectral Characteristics

The four spectral bands of the Landsat MSS are defined as follows (for historical reasons, they are num-

bered 4 through 7):

band 4: 500 - 600 nm
5: 600 - 700 nm
6: 700 - 800 nm
7: 800 - 1100 nm

In the absence of any documentation of the within-band spectral responses of the MSS, they are assumed to be flat: although this is surely not the case.

As can be seen from the O'Brien - Munis spectral reflectance curve (figure (3)), bands 4 and 5 contain largely redundant information. Bands 7 and (to a lesser extent) 6 span the spectral window where the transition from very high visible to very low infrared reflectance occurs. In the case of band 7, it would be desirable to have finer spectral resolution over an equivalent window, especially in view of the pronounced water vapor effects in this band (Dozier, 1979). It is additionally unfortunate that band 7, where most of the snow reflectance information is contained, has the least radiometric precision (6 bits, versus 7 bits for bands 4 through 6) and, historically, the least accuracy of the four MSS bands (NASA, 1977).

The combined spectral window of the MSS does not permit the discrimination of snow from clouds (Alfoldi,

1976), which can be a problem over a remote mountainous area where highly variable local weather conditions may not be well known. A satellite designed for snow monitoring would doubtless include a band further into the infrared (around 1600 nm), where the almost non-reflectance of snow contrasts with the highly-reflective water-droplet clouds (Barnes and Smallwood, 1975). The saturation ceiling of the bands in the visible portion of the spectrum would also need to be increased.

3.3.4. Temporal Characteristics

A single Landsat satellite will pass over most earth locations once every 18 days. If two Landsats are operating, their orbits are usually staggered so that the effective overpass interval is reduced to 9 days (however, as of this writing, only Landsat 3 is still operating). In itself, this interval is insufficient for snowpack albedo monitoring, for the following reasons:

- A single day's snow fall between overpasses can drastically increase the albedo of an existing snowpack. Conversely, a light snowfall just before the satellite overpass may deceptively increase both the albedo of the existing pack as well as its apparent spatial extent, only to disappear entirely days before the next overpass.

- During the ablation season, the change in albedo at the margins of a snowpack can be quite rapid (McGinnis, et al, 1975), especially in cases where decreasing depth causes the ground surface albedo to become significant.

For these reasons, supplementary information on the state of the snowpack is required. Extrapolation from a few spatially isolated field measurements over a complex topographic surface is inherently unsound. It may be possible, though, to monitor high-temporal-frequency events from sensors with significantly lower spatial resolutions, such as are carried by the NOAA/TIROS satellites (Algazi and Suk, 1975), and use these data to update the albedo model between MSS overpasses.

3.4. Atmospheric Effects in Irradiance and Exitance

The earth's atmosphere acts as a spectrally, spatially, and temporally variable filter to solar radiation. The two principal processes involved are absorption and scattering. Both processes will cause beam radiation to be attenuated. In addition, scattering introduces a diffuse radiation component, with entirely different geometric and spectral properties. With respect to the albedo model, atmospheric effects must be evaluated in converting the solar constant to surface irradi-

ance, and in deriving surface exitance from satellite radiometry.

3.4.1. Irradiance

The beam component of surface irradiance may be thought of as the product of the solar constant (i.e., the beam irradiance outside the earth's atmosphere) and an atmospheric transmission function. This transmission function is a composite of the optical behavior of both individual chemical compounds (e.g., water vapor; ozone), and atmospheric mixtures (e.g., Rayleigh and aerosol scattering). These individual transmission functions all vary with wavelength and atmospheric path length (which varies with the solar zenith angle and the elevation of the surface). Some of these transmission functions also vary because the atmospheric components whose behavior they describe are spatially and temporally variable. A model developed by Dozier (1979) employs transmission functions for ozone, water vapor, Rayleigh scattering, aerosol scattering, and miscellaneous gases. The spectral significance of each of these functions, for a "typical" set of atmospheric conditions, is shown in figure (8).

The diffuse component of irradiance derives from two sources: radiation which is scattered downward out of the incoming beam, and radiation which is reflected from the surface and subsequently "back-scattered" (Dozier, 1979). Downward scattering may be computed from the same transmission functions required for computing beam irradiance. Computations of backscattering require some information on the reflectance characteristics of the surface. The distinctive spectral reflectance of snow somewhat simplifies this problem (Dozier, 1979), for the purposes of the albedo model.

3.4.2. Exitance

There are two principal atmospheric effects in the composite earth-atmosphere signal which is measured by a spaceborne radiometer:

- path transmission: The atmosphere attenuates the surface upwelling radiance (i.e., the exitance in the direction of the satellite) in a manner similar to its effect on beam irradiance.
- path radiance: Due to scattering of beam and reflected solar radiation, there is a significant diffuse component in the direction of the satellite.

The combined effects of path radiance and transmission may be expressed as:

$$L\uparrow space[\lambda] = L\uparrow path[\lambda] + \tau[\lambda](Msurf[\lambda] / \pi) \quad (9)$$

Some of the problems inherent in determining path radiance and transmission are (Dozier and Frew, 1980):

- The Landsat MSS has a spectral resolution which is coarser than the spectral variations in both atmospheric attenuation and in snow surface reflectance. This makes it rather difficult to apply atmospheric corrections to MSS data.
- Both path transmission and path radiance vary with atmospheric parameters and with the elevation of the surface. In addition, path radiance will vary with the solar angle.
- With path transmission there is the problem of scattering in the upward direction, causing "smearing" of the radiance from one pixel over adjacent pixels.

4. Implementation of the Albedo Model

In this section the implementation of a surface albedo model according to the steps outlined in section 2.3 is discussed The resulting model is applied to a test site in the southern Sierra Nevada of California.

4.1. Bullfrog Lake Test Site

The test site selected for this investigation is a geodetic quadrangle centered on Bullfrog Lake, in the Bubbs Creek drainage of the South Fork of the Kings River

(see figure (9)). The Bullfrog Lake area was selected for the following reasons:

- The area selected is small (approximately 7.5 minutes square), yet contains both a wide range in elevations (2400 - 4200 m) and rugged topography. These properties yield a considerable variety of atmospheric and geometric radiation effects.

- Since most of the area is either a designated wilderness or a national park, and is inaccessible to casual travelers during the snow season, there are few artificial effects in the snow cover that need to be accounted for (e.g., packing by skiers and snowmobilers; air pollution; etc.).

- Kearsarge Pass (see figure (9)) affords relatively rapid (1 - 2 days) winter access to the study area by means of ski mountaineering. Teams of field investigators are thus able to make frequent field radiation measurements.

- Kings Canyon National Park has permitted the installation of an automatic Data Collection Platform (DCP) at Charlotte Ridge, between Bullfrog and Charlotte Lakes in the study area (see figure (9)). Instruments connected to the DCP include radiometers to obtain calibration data for the atmosphere models. The DCP consists of a solar battery, an analog-to-digital converter, a digital memory, and a programmable transmitter which samples and saves instrument readings at hourly intervals. The contents of the memory are relayed via the GOES satellite every six hours to a database in Washington, DC, which is interrogated daily by telephone.

4.2. Terrain Database

4.2.1. Elevation Data

A terrain base for the study area was created by first extracting a grid of elevations from the DTT corresponding to the eastern half of the Fresno 1:250,000 quadrangle. Misalignment of the original north-south transects was corrected. The grid spacing was reset to 100 m in both directions, both to cut down on the number of points required to cover the study area, and to filter out some of the high-frequency random noise. The logical structure of the grid was changed to row-major with the origin in the northwest corner, to more closely correspond to the image organization.

The positional and elevation errors of this data, and for others created for adjacent areas, were evaluated by Marks and Dozier (1979). For 30 points of known location and elevation, the RMS latitude, longitude, and elevation errors were all in the neighborhood of 50 - 60 m, or about one-half the grid spacing.

4.2.2. Geometric Radiation Calculations

Various topographic factors influence the distribution and flux density of irradiance (and therefore exi-

tance). Beam irradiance is locally influenced by slope and aspect, and by whether or not the solar beam is obscured by adjacent terrain (i.e., the local horizon). Diffuse irradiance is influenced by the distribution of terrain versus sky in the hemisphere above the calculation point (i.e., the terrain and sky view factors).

The following formulae are used to compute the slope and aspect at each elevation grid point (Dozier and Outcalt, 1979):

$$\text{slope} = \arctan(((\partial z/\partial x)^2 + (\partial z/\partial y)^2)^{(1/2)}) \quad (10)$$

$$\text{aspect} = \arctan((\partial z/\partial x) / (\partial z/\partial y)) \quad (11)$$

$\partial z/\partial x$ and $\partial z/\partial y$ are computed by finite-difference methods on the topographic grid, with a correction for latitude variations.

The horizon function is computationally complex but may be outlined as follows (after Dozier and Outcalt, 1979):

- Compare the current point [m,n] with every other point [i,j] in the grid. If z[i,j] <= z[m,n] then [i,j] is not a potential horizon for [m,n]; skip it.

- Compute the tangent of the horizon angle from [m,n] to [i,j]:

$$\tan(H) = (z[i,j] - z[m,n]) / (h^{**}2\ ((i-m)^{**}2 + (j-n)^{**}2))^{**}(1/2) \quad (12)$$

- Compute the sector number of [i,j] with respect to [m,n] (i.e., the "pie slice", centered at [m,n], in which [i,j] falls):

$$b[i,j] = \mathrm{int}(\arctan((j-n) / (i-m)) / w) \quad (13)$$

- Compare the current tan(H) with the previous tan(H)[b[i,j]]. If it is greater, then [i,j] is the new horizon for sector b[i,j].

- When all grid points have been tested, convert all (tan (H)[b] to zenith angles, and save them as a "horizon vector" for point [m,n].

Regardless of the number of sectors (w) used to construct the horizon vector (this investigation used 96; subsequent tests indicate that 32 are sufficient for radiation geometry calculations (Dozier, et al, 1980)), the procedure outlined above is of order (N**2) in computation time, since every grid point is compared to every other grid point. Even for small datasets this can lead to excessive computer time, since a considerable region outside the area of interest must be searched for possible horizon obstructions. On the other hand, the horizon

computations need only be done once, and can be saved for any subsequent analyses.

The terrain view factor (the fraction of the hemisphere above a point which is obscured by terrain) is computed by integrating the horizon function over an azimuth of 2π. For a discrete horizon vector, an approximation to this integral is given by (Dozier and Outcalt, 1979):

$$Vt[m,n] = \cos^2(\text{mean of horizon vector}[m,n]) \quad (14)$$

The sky view factor is then simply:

$$Vf[m,n] = 1 - Vt[m,n] \quad (15)$$

4.3. Space Radiance Data

The Bullfrog Lake study area falls in the southeast quadrant of Landsat path 45, row 34. The image used in this demonstration of the model was MSS frame 2753-1740000, acquired at 0940 PST on 13 February 1977. Coincident surface radiation measurements were obtained by a field party (Dozier et al, 1978a, vol. 2). The computer-"compatible"-tape (CCT) of the MSS image was re-

formatted, and a 256 line by 256 sample sub-image containing the test area was extracted (these dimensions are convenient for various display devices and are not an intrinsic requirement of the model).

4.3.1. Registration to Terrain Grid

MSS image transformations may be divided into two classes: rectification and registration (Van Wie and Stein, 1976). Rectification entails transforming the MSS data into a coordinate system which is a map projection (i.e., one which has a well-defined mathematical relationship to the geoid). It is usually possible to construct an analytical mapping between a particular map projection and the perspective projection which results when the systematic errors are removed from the MSS image. The remaining "random" (i.e., unexplained) error between image and map coordinates should be slight.

An accurate rectification, demands accurate map coordinates for the control points. This is not inordinately difficult over artificial landscapes, which typically present an abundance of point features with known geographic locations (e.g., field boundaries, highway intersections, small reservoirs, etc.). For remote wilder-

ness areas, map control points are much harder to obtain:

- Maps, when available, tend to be less accurate, less frequently updated, and of smaller scale than those of more populated areas.
- Point features such as mountain peaks or stream junctions are imprecisely located.
- In snow-covered areas, point features visible on maps are often buried and therefore invisible on the image.

For the particular application of this investigation, a rectfication procedure is inappropriate, since control points in a map coordinate system are difficult to obtain for the test area. Instead, the terrain grid is treated as an image to which the MSS data are registered. In a registration, or "rubber-sheeting", procedure, one image is declared the "target" (in this case, the terrain image) and all subsequent data are transformed to fit this target. Any intrinsic errors in the target image are ignored.

The procedure used to register the MSS data to the terrain grid may be outlined as follows:

- Locate control points in the image and in the terrain grid.
- Correct the image control point coordinates for selected systematic distortions.

- Compute a linear regression model which maps terrain grid coordinates into corrected image coordinates.
- Evaluate the regression model, followed by the inverse of the systematic distortion models, at each terrain grid point, yielding the image coordinates corresponding to that point.
- If the computed image coordinates do not correspond to an existing image location (which will almost certainly be the case), resample the image to assign an RN to those coordinates and thereby to the corresponding terrain grid point.

Control points in the terrain grid were located by generating a terrain "image" (essentially a shaded-relief map), in which the brightness value at each point represents the cosine of the solar zenith angle at that point, corrected for slope and aspect (Sellers, 1965):

$$\cos(Z') = \cos(S)\cos(Z) + \sin(S)\sin(Z)\cos(A - A') \quad (16)$$

The resulting image is similar to a shaded-relief map.

If Z and A are set to the solar zenith angle and azimuth for the date and time of the MSS overpass, then the resulting terrain image bears a close resemblance to the MSS image. The two images are then displayed simultaneously on a video monitor, and control points selected interactively by an addressable cursor. An effort was made to acquire an adequate number (20) of control points and

to distribute them fairly evenly over the test area, including some outside it, to help compensate for other inaccuracies in the registration procedure. Figure (10) contains a terrain image of a superset of the test area along with the MSS subimage of 13 February 1977 (which here has been subject to several systematic corrections, to facilitate the comparison).

Once the control points were located, selected systematic corrections were applied to their MSS coordinates. Of the systematic distortions mentioned in section 3.2.2, all but scan nonlinearity and sampling delay are continuous and linear over the entire image (or, in the case of panorama and earth curvature, over reasonably small subimages). These distortions were therefore not modelled, on the assumption that they would be easily compensated by the statistical transformation, and also because the spacecraft parameters required to compute them are imprecisely determined. For the test reported here, only a sampling delay correction was employed. The available scan nonlinearity models were developed for the (no longer operational) Landsat 1 MSS (Van Wie et al, 1975); and are of uncertain applicability to Landsat 2 (from which the test data were acquired). Remaining

"random" distortions were compensated by two first-order bivariate polynomials, whose coefficients were computed with the SAS "General Linear Models" multivariate regression program (Helwig and Council, 1979).

Resampling the MSS image presented severe problems due to the presence of numerous saturated pixels. These pixels cannot be included in a high-order interpolation kernel, since they do not represent bounded values. To preserve radiometric fidelity, zero-order (nearest neighbor) resampling was used to produce the registered image. Unfortunately, this method (a simple rounding of the predicted image coordinates to the nearest integer) introduces the greatest positional error of any resampling technique (Nack, 1977). Figure (11) shows a terrain image of the study area proper (a subset of the terrain image in Figure (10)), with a registered MSS band 5 image.

4.4. Irradiance Simulation

The irradiance simulation model used in this investigation is described in Dozier (1979). The model is quite involved; therefore, only an overview of its workings is presented in this section. Both beam and diffuse irradiance are simulated. The model is monochromatic, so

for this application, the results were integrated over the wavelength ranges of the MSS bands. The irradiance simulation is run prior to the surface exitance derivation, because one of the by-products of the irradiance simulation is a set of atmospheric parameters which the exitance model requires.

4.4.1. Overview of the Irradiance Model

Beam irradiance (on a surface normal to the solar beam) is computed by correcting the solar constant for the following:

- earth-sun distance
- atmospheric absorption (by ozone, water vapor, aerosols, and miscellaneous gases)
- atmospheric scattering (Rayleigh and aerosol)

Of the physical factors governing these effects, the following atmospheric parameters cannot be determined a priori, and therefore must be derived from field measurements:

- ozone content
- precipitable water vapor
- aerosol attenuation coefficient

The aerosol attenuation coefficient is determined from the Angstrom turbidity function, which is governed by two parameters (α and β). Of these, the β parameter is most sensitive to atmospheric aerosol content and is thus derived from field measurements.

Diffuse irradiance is separated into scattered (out of the solar beam) and backscattered (from surface exitance) components. The amount of radiation scattered out of the solar beam can be determined from the previously-computed Rayleigh and aerosol scattering functions. If it is assumed that scattering takes place at a single altitude (in this model, z such that P[z] = P[sfc] / 2), then the amount of the scattered radiation which reaches the surface can be determined from the previously-computed absorption functions. The respective quantities of these absorbers are corrected for the amount of atmosphere between z[sfc] and z[P[sfc]/2].

Backscattered irradiance is computed from the beam and scattered diffuse irradiances already derived, multiplied by an assumed regional albedo. This is not to be confused with the albedo of the point itself, and in fact the model is not very sensitive to this parameter. This

investigation used the O'Brien - Munis "reference" snow reflectance curve for a regional albedo (see figure (3)). This computation yields a regional exitance which is corrected for attenuation on either branch of its round trip to the scattering level z[P[sfc]/2]. The necessary absorption and scattering functions have at this point already been computed.

Finally, in regions of high relief such as the test area of this investigation, there is significant diffuse irradiance due to reflection from adjacent terrain. Reflected diffuse radiation is computed by multiplying the regional exitance by the terrain view factor. Diffusely-reflected beam radiation is obtained by averaging calculations for each sector in the horizon vector for the point. Specularly-reflected beam radiation from adjacent terrain is not considered. To do so would add greatly to the computational complexity of the model; and in any case the likelihood of the ocurrence of the particular orientation of the sun and the two opposing slopes required to achieve a significant specular reflectance, is intuitively quite small (see section 4.6).

The "unknowns" in the model (atmospheric ozone con-

tent, precipitable water vapor, Angstrom β coefficient) are derived from field measurements, taken at different times during the day so as to include differing atmospheric path lengths for the beam irradiance. Since there are three unknowns, at least three measurements are required, with four or more being preferred to obtain the redundancy needed for estimating measurement error. The measurements are assumed to be the output of the simulation model, which is then solved inversely for those values of the unknown coefficients which would have generated the observed irradiances. These parameters may then be used to run the model for any specific time (or integrated time interval) during that day.

Figure (12) is an irradiance "image" generated on the test area terrain grid for MSS band 5, for the time of the Landsat overpass on 13 February 1977.

4.5. Surface Exitance Derivation

By applying equation (8) to the registered MSS data, a space upwelling radiance value is obtained for each terrain grid point, for up to four MSS bands (many points will have less than four bands of information due to saturation). The conversion of the values into surface ex-

itance requires corrections for the atmospheric path radiance and transmission effects described in section 3.4.2. Procedures for computing these corrections are developed in Dozier and Frew (1980), and are outlined briefly below.

Path radiance is computed by essentially the same method as scattered diffuse irradiance, since they both derive from scattering of the solar beam (assumed to occur at z[P[sfc]/2]). In the case of path radiance, the absorption functions are evaluated from the scattering altitude up to the top of the atmosphere, rather than down to the surface as was the case in the diffuse irradiance simulation. The resulting value is a diffuse atmospheric exitance, which is converted to radiance by multiplying by π.

Figure (13) shows path radiance as a function of wavelength for different atmospheric aerosol and water vapor contents, respectively. The four curves in each graph represent two different dates each evaluated for two different altitudes. The significance of the path radiance correction, especially over rugged terrain, should be apparent.

The path transmission correction requires some knowledge of the relative spectral reflectance of the surface. For a snowpack, the O'Brien - Munis curve (figure (3)) is used, since spectral signature of snow is fairly constant over time. By combining this postulated surface reflectance, the previously simulated irradiances, and equation (9), a surface exitance can be computed which is spectrally, although not radiometrically, correct. This "pseudo-exitance" is subject to scattering at z[P[s↑c]/2]. The sum of the portion which is not scattered, and the fraction of the scattered portion which reaches space, constitutes the surface exitance component of the signal which is perceived at the MSS. Equation (9) may thus be rewritten:

$$\tau[\lambda] = \pi(L\uparrow sc[\lambda] + L\uparrow direct[\lambda])/Msurf[\lambda] \qquad (17)$$

Integrating with respect to λ over the spectral range of an MSS band causes the radiometric units to cancel, leaving a τ[band] which is basically a function of altitude.

Combining path radiance and transmission gives the following equation for surface exitance:

$$M[band]surf = \pi(L\uparrow space[band] - L\uparrow path[band])/\tau[band] \quad (18)$$

This was implemented as a pointwise algebraic combination of images of space radiance, path radiance, and path transmission, generated for the date and time of the Landsat overpass. Figure (14) contains path radiance and transmission images for MSS band 5. Compare these with the pseudo-relief terrain image in figure (11), and note the variations of both phenomena with altitude.

4.6. Derivation of Surface Albedo Components

In section 3.1.3, it was noted that the albedo of a snow-covered surface has three components (f, ρ, and ρ'), which must each be known if the surface energy balance is to be calculated from irradiance and albedo alone. This section presents methods for calculating these components.

It can be shown geometrically (see figure (15)) that the surface exitance derived from MSS data will not include a measurable specular reflectance. Instead, specular reflectance is computed by using the index of refraction for ice (approximately 1.3 for solar wavelengths; from Irvine and Pollack, 1968), and averaging the result-

ing plane- and cross-polarized Fresnel reflectances (Sellers, 1965):

$$f = .5((\sin^2(Z' - ar)/\sin^2(Z' + ar) + \tan^2(Z' - ar)/\tan^2(Z' + ar)) \quad (19)$$

where:

$$ar = \arcsin(\sin(-Z')/ir);\ ir = 1.3 \quad (20)$$

Note that f is strictly a function of the angle of incidence of the beam irradiance. Figure (6) contains a graph of f versus Z; note that at all but very large zenith angles, f is insignificant.

The surface exitance derived from MSS data is related to surface reflectance by:

$$M = \rho' Ed + \rho[Z]Es \quad (21)$$

The omission of λ here is deliberate, since the MSS data are integrated over a fairly broad range of wavelengths. A result of this integration over the differing spectral distributions of Ed and Es is that ρ' is not the same as $\rho[0]$, for a given MSS band. However, since the transmission functions which govern the spectral distributions of

Ed and Es are functions of elevation, we can postulate the following relationship:

$$\rho[0]/\rho' = Es/Ed = C[z] \qquad (22)$$

C[z] is determined for the range of elevations in the test area as follows:

- Collect values of ρ' for a range of elevations by ratioing exitance and irradiance in areas shaded by terrain from beam irradiance.
- At these same elevations, select locations which are exposed to the solar beam. The difference in exitance will be due to $\rho[Z']$, which can be corrected to $\rho[0]$ using a variation of equation (6).
- Compute and save C values for these elevations. At other elevations, find C by interpolation.

Combining equations (6), (21), and (22) gives the following expression for ρ':

$$\rho' = (M - Es(g[Z] + f[Z])) / (Ed + EsC[z](1 - g[Z])) \qquad (23)$$

Figure (16) contains images of ρ' for MSS bands 5 and 7. The apparently incongruous black spots were saturated pixels in the original MSS data.

4.7. Spectral Albedo Extension

The procedure derived above cannot be applied directly if exitance information is unavailable due to saturation of the MSS data. This problem ranges from severe in bands 4 and 5 to negligible in band 7 (see figure (16)), as might be predicted from prior knowledge of the spectral reflectance characteristics of snow. What is needed is a method of indirectly deriving the albedo in the saturated bands.

The spectral extension method depends on the fact that, because of band 7, there is at least one spectral band of exitance (and therefore albedo) information for the entire image. Recall from section 3.1.2 that natural variations in the overall albedo of snow can be closely approximated by a multiplicative adjustment of a spectrally correct reflectance curve (e.g., figure (3)). For example, if a monochromatic reflectance measurement ($\rho[\lambda]$) is made of a "patch" of snow, the factor by which the reference spectral reflectance curve must be multiplied to yield the measured value is given by:

$$K = \rho[\text{measured}]/\rho[\text{reference}] \qquad (24)$$

This K value may then be applied to any ρ[λ] on the reference curve to yield a best estimate of the actual reflectance that would have been measured at that wavelength.

For a spectrally broadband reflectance measurement, such as is derived from the MSS data, the measured reflectance is ratioed with the integrated value of the reference curve for the same wavelength interval:

$$K = \rho[band]/\rho[reference]\ d\lambda \qquad (25)$$

The K-value thus computed has twofold utility. First, it may be used outside the spectral range for which immediate measurements are available, as long as it is within the range of the reference curve from which it was derived. Second, the K-value is a unique determinant of spectral reflectance of a given snow-covered point, and thus is the only value which need be saved, as long as the reference curve is available to reconstruct the reflectances. This represents up to a 4x data reduction, which can be quite significant for large areas.

Figure (17) shows an MSS band 5 image with the sa-

turated values reconstructed from K-values computed from band 7 exitances and the O'Brien - Munis reference snow spectral reflectance curve.

5. Analysis and Conclusion

In this section, each phase of the albedo model will be examined with respect to potential sources of error which could contribute to the accuracy of the final results.

5.1. Terrain data

The inaccuracies inherent in the digital terrain data distributed as DTTs have already been discussed. The general effect of these errors would be to introduce isolated singularities in the derived terrain data. For example, the misplacing of a cliff by one grid point would cause the derived parameters in that immediate neighborhood to be grossly inaccurate. While such errors tend to cancel out in the context of an energy balance model evaluated over tens or hundreds of thousands of points, they can cause errors in situations where point-specific data are disproportionately critical. Two instances of this are registration control points and loca-

tions of field measurements

Errors in registration control point locations can be alleviated by using an excessive number of points to derive the registration transformation. If the positional errors of the points are not systematic, this should cause most of the errors to cancel out. Wildly inaccurate control points, such as might result from a misplaced mountain peak, can usually be detected by "cross-checking" (Van Wie et al, 1975). This entails predicting the location of each control point using a model derived from the remaining control points. A poorly located point will be indicated by large absolute or standard errors in its estimated location.

Errors in locating field measurements arise due to the various locational transformations they undergo (a measurement made in the field is marked on a map; its geodetic coordinates are manually measured; the geodetic coordinates are used to derive an [x,y] location in the terrain grid). These errors can be reduced by visually inspecting the terrain grid neighborhood of the derived field location, by means of a pseudo-relief image, a numeric printout of the elevation grid, and/or a contour

map. Persons familiar with the field area can usually recognize sufficient cues from such displays to "fine tune" the measurement locations.

5.2. Landsat MSS Data

Use of Landsat MSS data in this model is subject to the following errors:

- inaccurate space radiance values due to calibration errors in the MSS system.
- positional errors due to resampling.
- spectral averaging by the relatively broad MSS bands.
- spatial averaging of subpixel-frequency terrain effects.

The absolute calibration of the MSS system is plainly inadequate, as can be qualitatively deduced from the striping which appears in almost all MSS imagery. Some idea of the magnitude of this variation may be gained from table (2), which shows the mean values for all of the detectors, organized by band, for the raw MSS subimage from which the registered data used in this investigation were extracted. The maximum mean within-band interdetector variation observed was 1.47 RNs in band 6.

The positional inaccuracy of nearest neighbor resampling, mandated by the occurrence of saturated pixels, doubtless leads to some mismatch of MSS data with terrain and irradiance information. Although, ideally, the extent of this error is no more than ± one-half pixel, in practice nearest-neighbor resampling tends to magnify any errors in the registration transformation (Taber, 1973).

Spectral averaging refers to the masking of sharp fluctuations in the spectral response of the surface and/or atmosphere, by the relatively broad spectral range over which a single MSS band is integrated. Examination of typical curves for snow spectral reflectance (figure (3)) and atmospheric spectral transmission (figure (8)) show that spectral averaging is most significant in band 7. This is due in part to the fact that this band has three times the spectral range of the other MSS bands, but mainly to the rapid change in snow albedo at these wavelengths and the atmospheric water vapor absorption bands. Compounding this problem is that for portions of a snow-covered scene, only band 7 will be unsaturated, so this band will be relied on more than the others.

The effective IFOV of the MSS translates to about 56

by 79 m at the surface (about 1.1 acre). Any changes in surface parameters which occur at a higher spatial frequency will be confused (aliased) by the MSS system. An example of this situation is the mistaking of patches of snow interspersed with bare ground or rock, for a uniform "dark" snow cover. Furthermore, the surface area per pixel increases with the slope of the surface, so that phenomena whose spatial frequency approaches the resolution limits of the MSS may affect "steep" pixels more than "level" ones.

5.3. Atmospheric Corrections

Errors in the irradiance simulation and in the surface exitance derivation may result from improperly specified atmospheric parameters. These in turn result from errors in the field measurements, and from spatial variations in atmospheric parameters assumed constant.

Field measurements have presented some problems in this investigation. The portable radiometers carried into the back country by the investigators have yielded some plainly erroneous measurements, such as irradiances which increase with increasing solar zenith angle, or irradiances in excess of the solar constant. The portion

of the irradiance model which derives the atmospheric parameters from these measurements can cope with some degree of measurement error, but in several cases the field measurments have proven unusable. The most accurate and reliable results have been obtained from Eppley pyranometers running continuously and unattended at the DCP.

Even with usable mobile field measurements, only a small portion of the test area can be covered for a given satellite overpass. It is assumed that the principal atmospheric parameters being derived (water vapor absorption and aerosol scattering) have a predictable variation vertically and no variation horizontally. For the Bullfrog Lake test area this assumption is valid, owing to the high elevation of the area and its remoteness from any sources of artificial air pollution. Indeed, the most significant impact on the assumption of spatial invariance would occur in cases of fires in or near the study area. Fortunately, such events are quite rare in the snow season.

5.4. Surface Conditions

Errors in this category constitute a catch-all of possible violations of the fundamental assumption of the model; namely, that every point in the terrain grid is covered exclusively with a reasonable depth of snow. In a mountainous area this is almost certainly not true, if for no other reason than that some slopes will be too steep to sustain a snowpack. The model presented here does not address itself to this class of problems; rather, the assumption is made that separate mechanisms exist to determine which grid points are snow-covered and which are not. In fairness to the model, it should be noted that the the errors involved in calculating a snow albedo for a non-snow point are significant mainly in subsequent energy-balance calculations, and will not cause severe error propagation within the model itself. This is due to the relative insensitivity of those calculations which rely on regional rather than point reflectances.

A more subtle problem arises when the surface consists not of smooth snow (or smooth non-snow mistaken for snow), but instead of a mixture of snow and trees. Such a mixture is significant since it radically affects the

radiation geometry of a neighborhood of grid points. A simple means of avoiding the problem would be to prepare a mask (based on, say, classified summer MSS imagery) showing for each grid point the presence or absence of sufficiently dense vegetation to affect the model.

5.5. Conclusions and Further Work

The model developed in this investigation is computationally complex but not prohibitively so; and the information it yields is otherwise unavailable. A detailed check of its overall accuracy has not been performed; however, its principal components have been demonstrated to perform adequately. The overall strategy of the model is based on fundamental physical principles (i.e. it is deterministic rather than statistical). The model's principal limitation is its pervasive reliance on the known spectral characteristics of the surface, which, while an acceptable approach for snow, may be more difficult to apply over spectrally heterogeneous surfaces. The field measurements required are kept to an absolute minimum. The model is not intrinsically dependent on Landsat MSS data; indeed, it would doubtless benefit from spaceborne radiometry with wider dynamic range, narrower

and better-defined spectral bands, less geometric distortion, and more frequent overpasses. The other data inputs are similarly general in that they can be upgraded to state-of-the-art as desired.

Further development of the model should include a field test of its accuracy. The two major factors which have so far prohibited such a test are the remoteness of the study area, and the infrequency of Landsat overpasses. The mountaineering skill required to enter the study area in the winter, combined with the limited load a person on skis can carry, has effectively limited the number of people and instruments which can be on-site during a satellite overpass. Moreover, it is neither feasible nor desirable to remain in the study area for the 18 days between Landsat overpasses, while the cost of frequent separate trips becomes prohibitive.

A field test could possibly be implemented using NOAA satellite data and a more accessible test area. Work is currently in progress to integrate AVHRR data into the terrain/radiation database scheme described in this paper. The daily coverage afforded by the NOAA AVHRR (Advanced Very High Resolution Radiometer) would

allow the field investigators the option of remaining at a particular site for several consecutive overpasses, or moving to different sites for each overpass, thus sampling a maximum variety of surface conditions. The coarse spatial resolution of the AVHRR (900 m) would probably require a test area with less relief than the current one, so that spatial averaging effects would not be immediately blamed for any inaccuracies in the model. Techniques such as spectral analysis of the digital terrain database may prove useful in recognizing areas where the spatial frequency of surface relief would lead to significant averaging or aliasing errors.

REFERENCES

Ad Hoc Advanced Imagers and Scanners Working Group (1973) Advanced Scanners and Imaging Systems for Earth Observations. Washington, D.C. : NASA SP-335. 604 pp.

Alfoldi, Thomas T. (1976) Digital analysis of Landsat MSS imagery for snow mapping applications. Canada Centre for Remote Sensing. 21 pp.

Algazi, V. Ralph; Suk, Minsoo (1975) An all-digital approach to snow areal mapping and snow modeling. In: Rango, Albert (ed.) Operational Applications of Satellite Snowcover Observations. Washington, DC : NASA SP-391. pp. 249-257.

Anderson, Eric A. (1976) A point energy and mass balance model of a snow cover. Washington, DC : NOAA Tech. Rept. NWS-19. 150 pp.

Barnes, James C.; Smallwood, Michael D. (1975) Synopsis of current satellite snow mapping techniques, with emphasis on the application of near-infrared data. In: Rango, Albert (ed.) Operational Applications of Satellite Snowcover Observations. Washington, DC : NASA SP-391. pp. 199-213.

Bergen, James D. (1975) A possible relation of albedo to the density and grain size of a natural snow cover. Water Resources Research 11: 5, 745-746.

Bernstein, Ralph; Ferneyhough, Dallam G., Jr. (1975) Digital image processing. Photogramm. Engr. 41: 12, 1465-1476.

Choudhury, B.J.; Chang, A.T.C. (1979) Two-stream theory of the spectral reflectance of snow. IEEE Trans. Geoscience Electronics GE-17: 3, 63-68.

Dirmhirn, Inge; Eaton, Frank D. (1975) Some characteristics of the albedo of snow. Jour. Appl. Meteorol. 14: 3, 375-379.

Dozier, Jeff; Davis, Robert; Frew, James; Gold, Caryn; Keith, Sandra; Marks, Danny (1978a) Remote sensing applications to hydrologic modeling in the southern Sierra Nevada and portions of the San Joaquin Valley (2 vols.) (final report, NASA grant NSG-5155). University of California, Santa Barbara, CA : Department of Geography.

Dozier, Jeff; Davis, Robert; Frew, James; Marks, Danny (1978b) Calibration of satellite data for input to distributed parameter hydrologic models. University of California, Santa Barbara, CA : Computer Systems Laboratory Technical Report TR-CSL-7808.

Dozier, Jeff (1979) A solar radiation model for a snow surface in mountainous terrain. In: Colbeck, S.C. (ed.) Workshop on Modeling Snow Cover Runoff. Hanover, NH : U.S. Army Cold Regions Research and Engineering Laboratory.

Dozier, Jeff; Outcalt, Sam I. (1979) An approach toward energy balance simulation over rugged terrain. Geographical Analysis 11: 1, 65-85.

Dozier, Jeff; Bruno, John; Downey, Peter (1980) A faster solution to the horizon problem. Computers and Geosciences, in press.

Dozier, Jeff; Frew, James (1980) Atmospheric corrections to satellite radiometric data over rugged terrain. University of California, Santa Barbara, CA : Computer Systems Laboratory Technical Report no. TR-CSL-7909, 35 pp.

Dunkle, Robert V.; Bevans, J.T. (1956) An approximate analysis of the solar reflectance and transmittance of a snow cover. Jour. Meteorol. 13: 212-216.

Feynman, Richard P.; Leighton, Robert B.; Sands, Matthew (1963) The Feynman Lectures on Physics, vol. 1. Reading, Mass. : Addison-Wesley.

Giddings, J.C.; LaChapelle, E. (1961) Diffusion theory applied to radiant energy distribution and albedo of snow. Jour. Geophys. Res. 66: 1, 181-189.

Helwig, Jane T.; Council, Kathryn A. (eds.) (1979) SAS User's Guide. Raleigh, NC : SAS Institute, Inc. 494 pp.

Hobbs, Peter V. (1974) Ice Physics. London : Oxford University Press. 837 pp.

Hubley, Richard C. (1955) Measurements of diurnal variations in snow albedo on Lemon Creek Glacier, Alaska. Jour. Glaciol. 2: 18, 560-563.

Irvine, William M.; Pollack, James B. (1968) Infrared optical properties of water and ice spheres. Icarus 8: 2, 324-360.

Kirby, M.; Steiner, D. (1978) The appropriateness of the affine transformation in the solution of the geometric base problem in Landsat data. Canadian Jour. Rem. Sens. 4: 1, 32-43.

Marks, D.; Dozier, J. (1979) A clear-sky longwave radiation model for remote alpine areas. Arch. Meteorol. Geophys. Bioklim., Ser. B 27: 159-187.

McGinnis, David F., Jr.; McMillan, Michael C.; Wiesnet, Donald R. (1975) Factors affecting snow assessment from Landsat data. NASA Earth Resources Survey Symposium 1-D: 2661-2668.

Middleton, W.E.K.; Mungall, A.G. (1952) The luminous directional reflectance of snow. Jour. Opt. Soc. Amer. 42: 8, 572-579.

Nack, M.L. (1976) Rectification and registration of digital images and the effect of cloud detection. Symposium on Machine Processing of Remotely Sensed Data, pp. 12-23. West Lafayette, IN : LARS, Purdue University.

NASA (1971) ERTS Data Users Handbook. Greenbelt, MD : GSFC Document no. 71SD4249.

NASA (1976) Landsat Data Users Handbook. Greenbelt, MD : GSFC Document no. 76SDS4258.

NASA (1977) Radiometric calibration of Landsat 2 MSS data. Landsat Newsletter 15: 1-2.

O'Brien, Harold W.; Munis, Richard H. (1975) Red and near-infrared spectral reflectance of snow. Hanover, NH : U.S. Army Cold Regions Research and Engineering Laboratory Research Report 332. 18 pp.

O'Neill, A.D.J.; Gray, Don M. (1973) Spatial and temporal variations of the albedo of prairie snowpack. The Role of Snow and Ice in Hydrology 1: 176-186. Geneva, Switzerland : International Association of Hydrologic Sciences.

Paltridge, G.W.; Platt, C.M.R. (1976) Radiative Processes in Meteorology and Climatology. Amsterdam : Elsevier Scientific.

Perla, Ronald I.; Martinelli, M. (1975) Avalanche Handbook. Washington, DC : USDA Agriculture Handbook 489. 238 pp.

Petzold, D.E. (1977) An estimation technique for snow surface albedo. McGill Univ. Climatol. Bull. 21: 11 pp.

Sellers, William D. (1965) Physical Climatology. Chicago, IL : University of Chicago Press. 272 pp.

Taber, John E. (1973) Evaluation of digitally corrected ERTS images. Third ERTS-1 Symposium 1-B: 1837-1844.

Thomas, Valerie L. (1975) Generation and physical characteristics of Landsat 1 and 2 MSS computer compatible tapes. Greenbelt, MD : NASA/GSFC X-563-75-233, 28 pp.

U.S. Army Corps of Engineers (1956) Snow Hydrology. Portland, OR : 437 pp.

U.S. Geological Survey (1979) Landsat Data Users Handbook, revised edition. Arlington, VA.

Van Wie, P.; Stein, M.; Puccinelli, E.; Fields, B. (1975) Landsat Digital Image Rectification System preliminary documentation. Greenbelt, MD : GSFC Information Extraction Division.

Van Wie, Peter; Stein, Maurice (1976) A Landsat digital image rectification system. Symposium on Machine Processing of Remotely Sensed Data, pp. 4a18-4a26 West Lafayette, IN : LARS, Purdue University.

Wiesnet, Donald R.; McGinnis, David F.; McMillan, Michael C. (1974) Evaluation of ERTS-1 data for certain hydrologic uses (final report, NASA contract no. 432-641-14-04-03). Greenbelt, MD : Goddard Space Flight Center.

Wong, Kam W. (1975) Geometric and cartographic accuracy of ERTS-1 imagery. Photogramm. Engr. 41: 5, 621-635

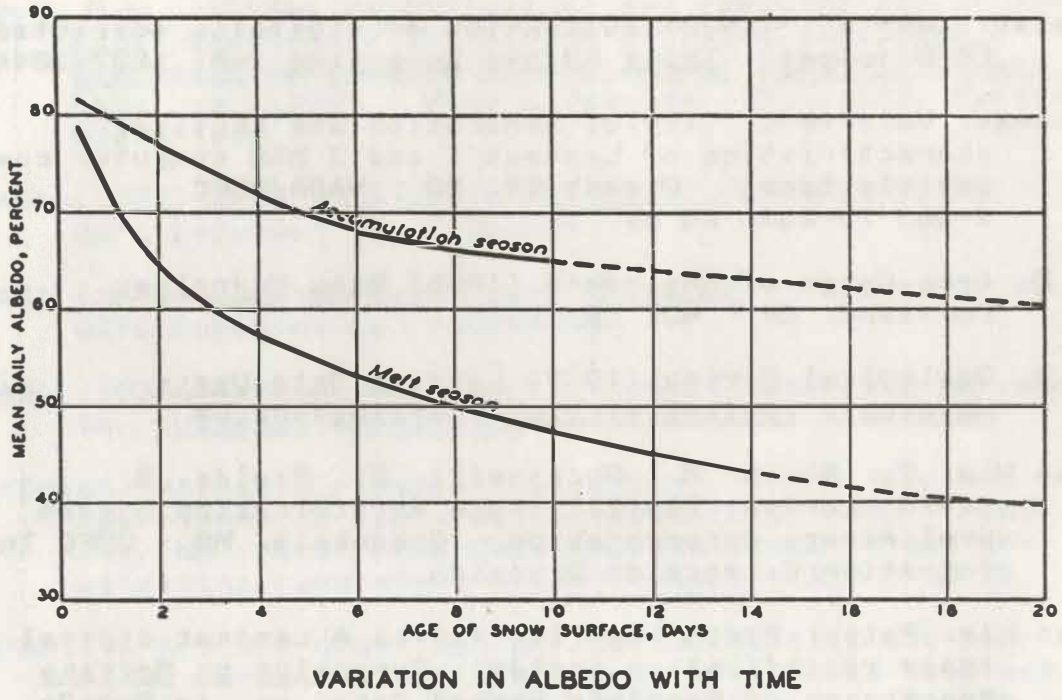

Figure 1: temporal decay in snowpack albedo, from in-situ measurements (U.S. Army Corps of Engineers, 1956).

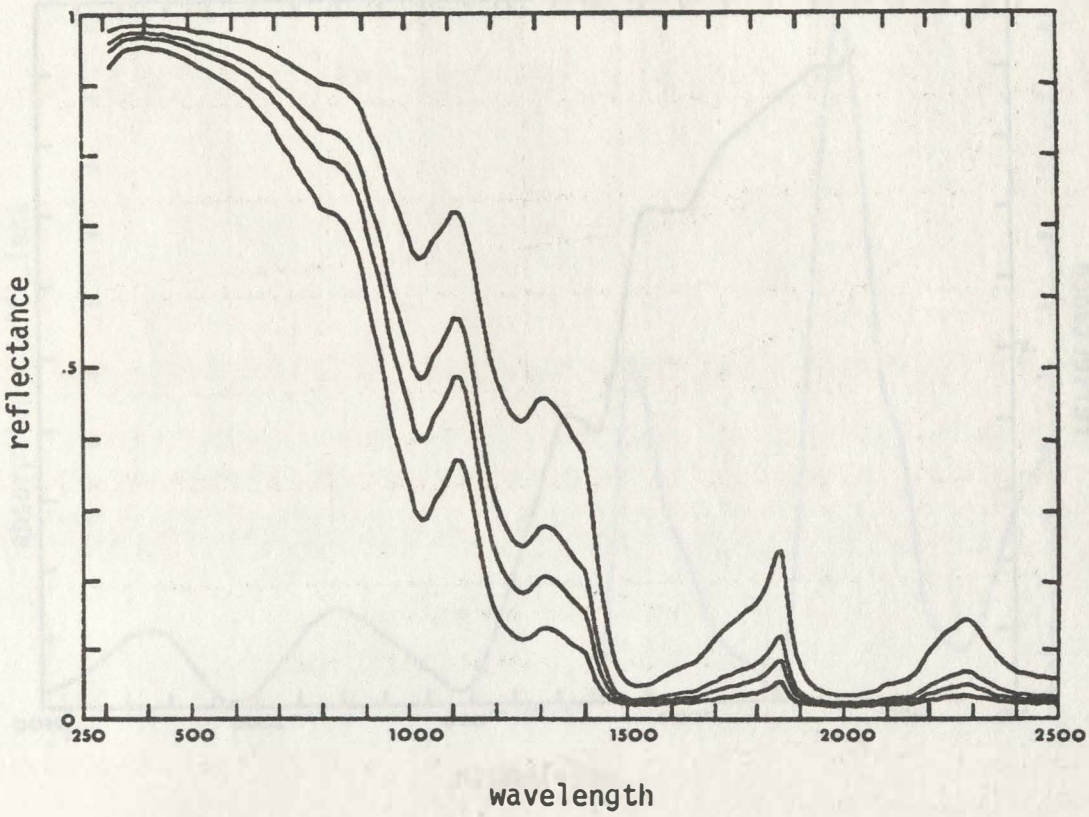

Figure 2: snow spectral reflectance generated for various grain sizes (model from Dunkle and Bevans, 1956).

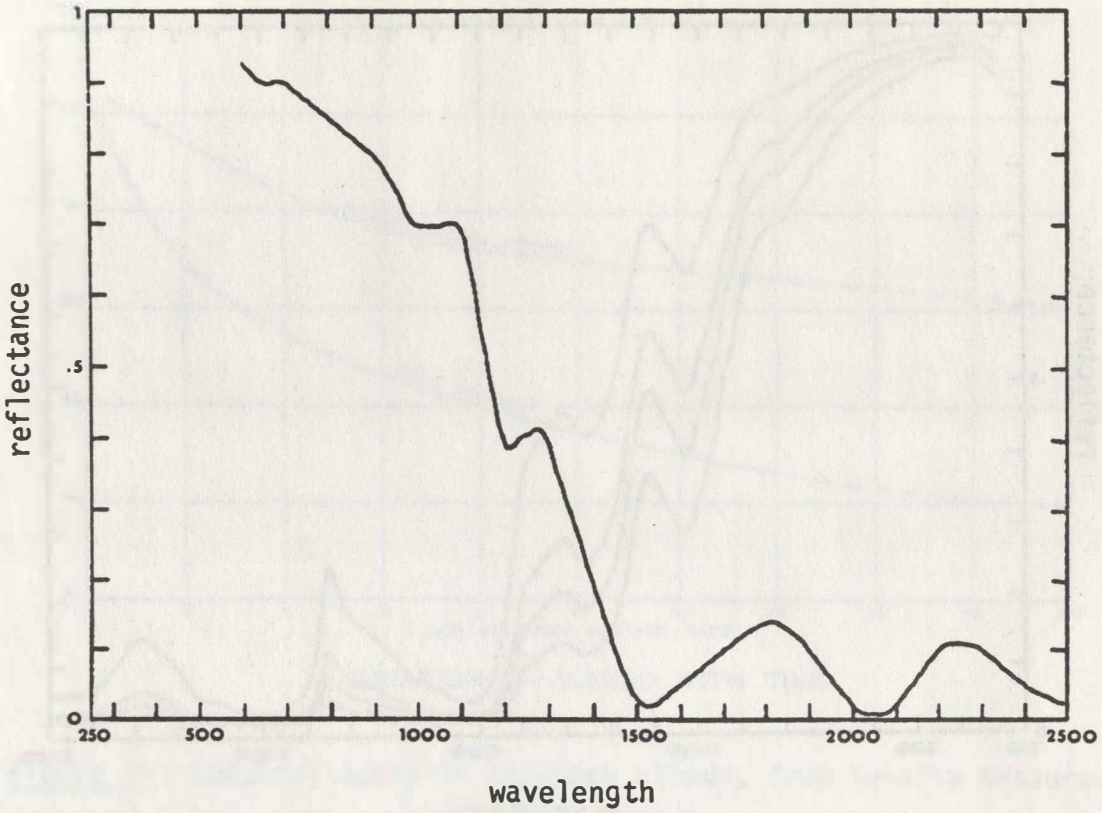

Figure 3: "typical" measured spectral reflectance of new snow, relative to $BaSO_4$ (data from O'Brien and Munis, 1975).

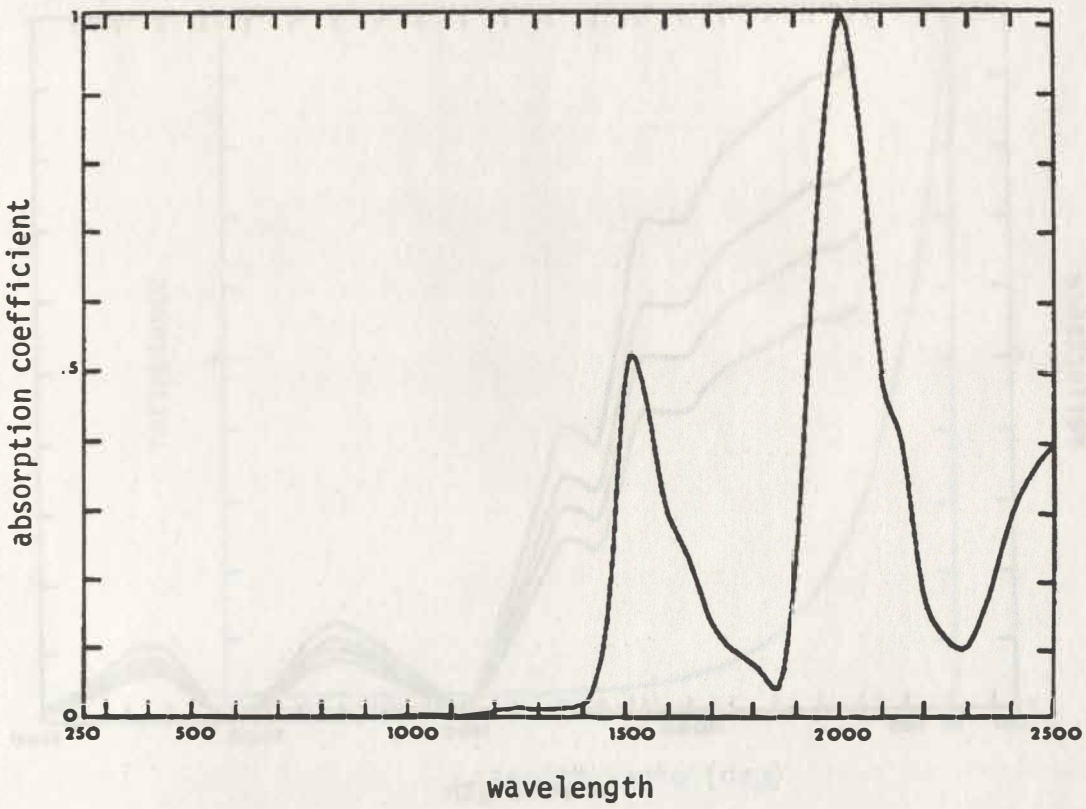

Figure 4: spectral absorption coefficient of ice (data from Irvine and Pollack, 1968; Hobbs, 1974).

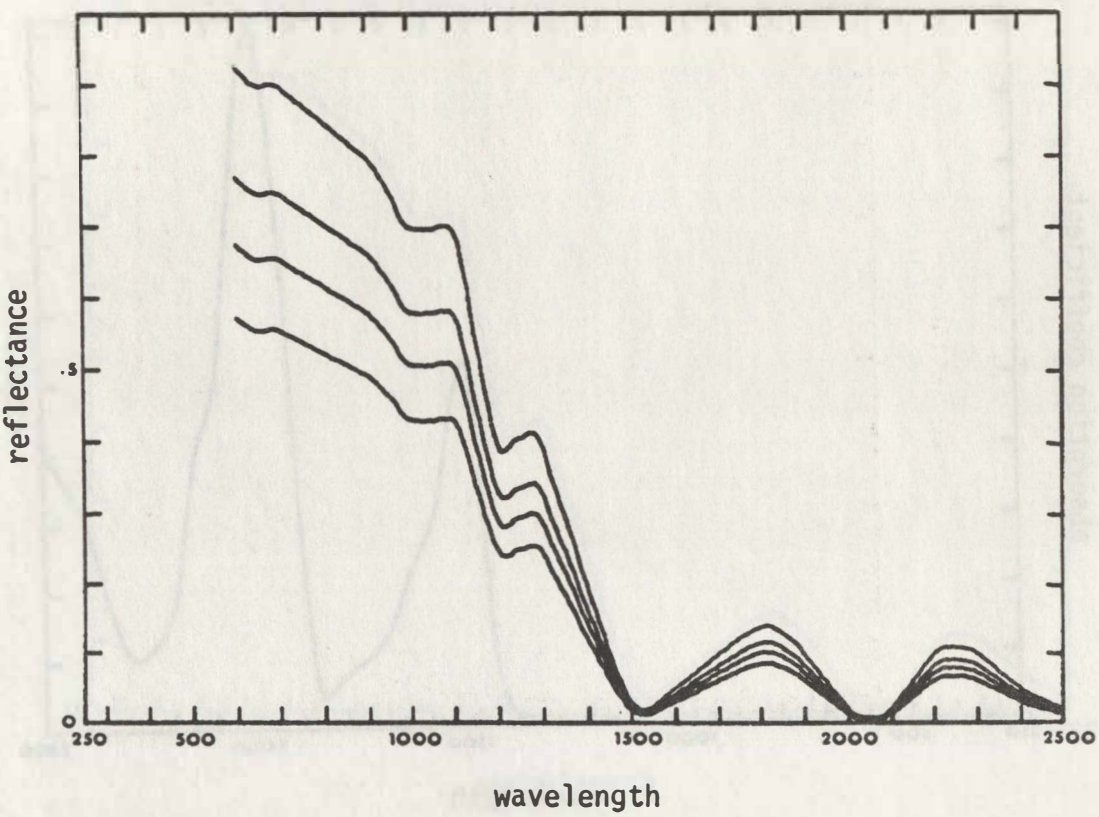

Figure 5: simulated temporal decay in snow spectral reflectance, generated by multiplying the curve in Figure (3) by various constant values.

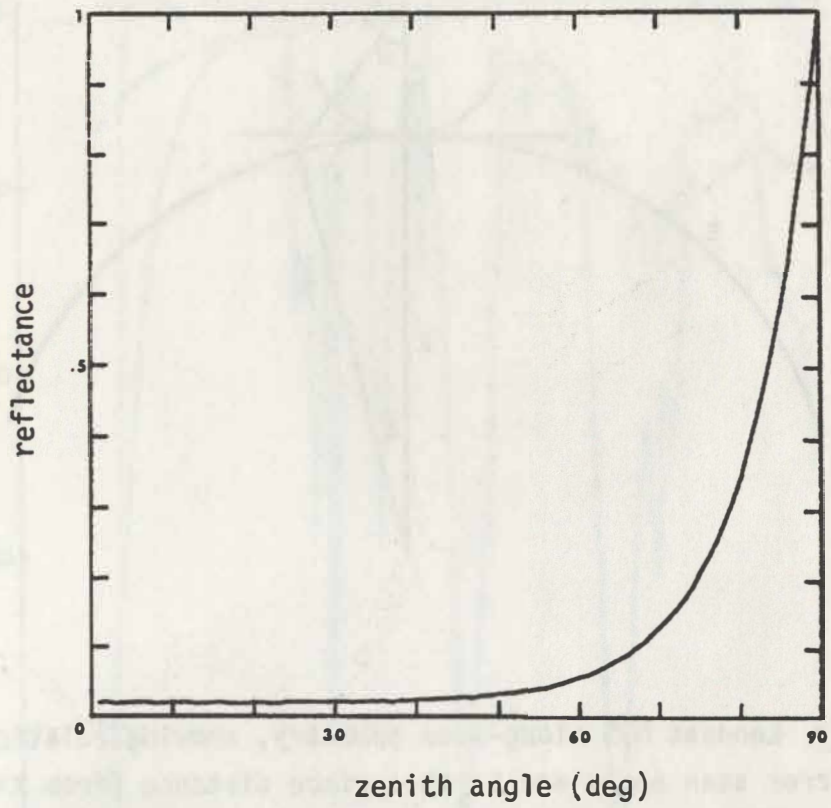

Figure 6: Fresnel (specular) reflectance of ice as a function of beam angle of incidence.

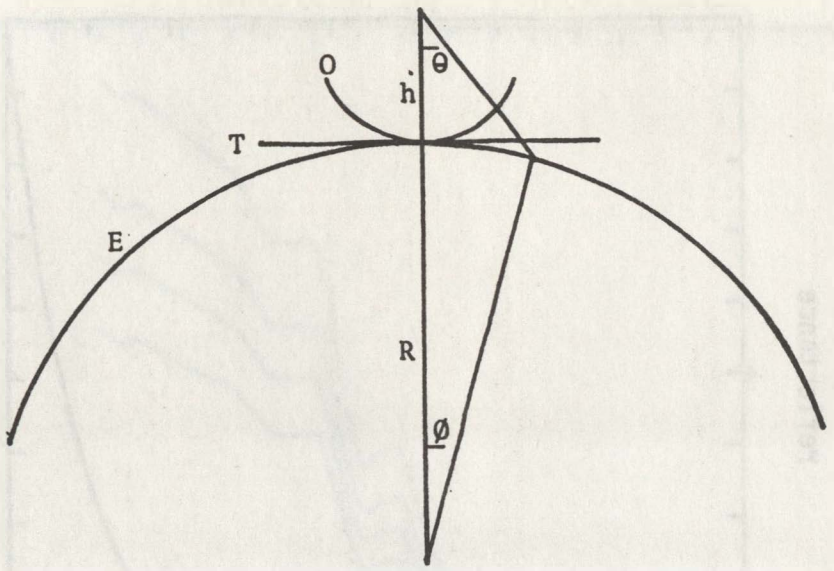

Figure 7: Landsat MSS along-scan geometry, showing relation between mirror scan angle and Earth surface distance (from Kirby and Steiner, 1978).

Parameters

h = altitude of MSS
θ = MSS mirror scan angle (from nadir)
O = MSS object plane
T = tangent plane
E = Earth surface
R = earth radius
Ø = geocentric angle resulting from a given θ

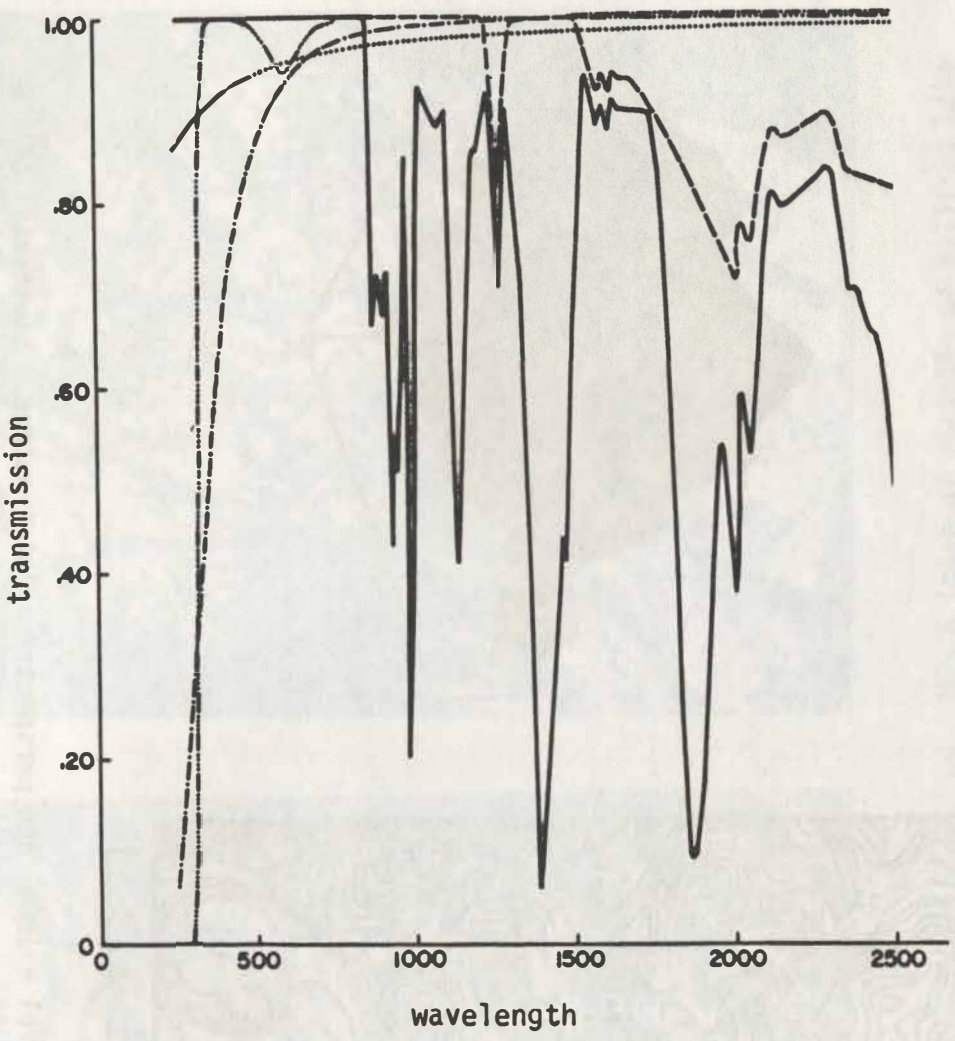

Figure 8: spectral absorption characteristics of various atmospheric constituents (Dozier, 1980).

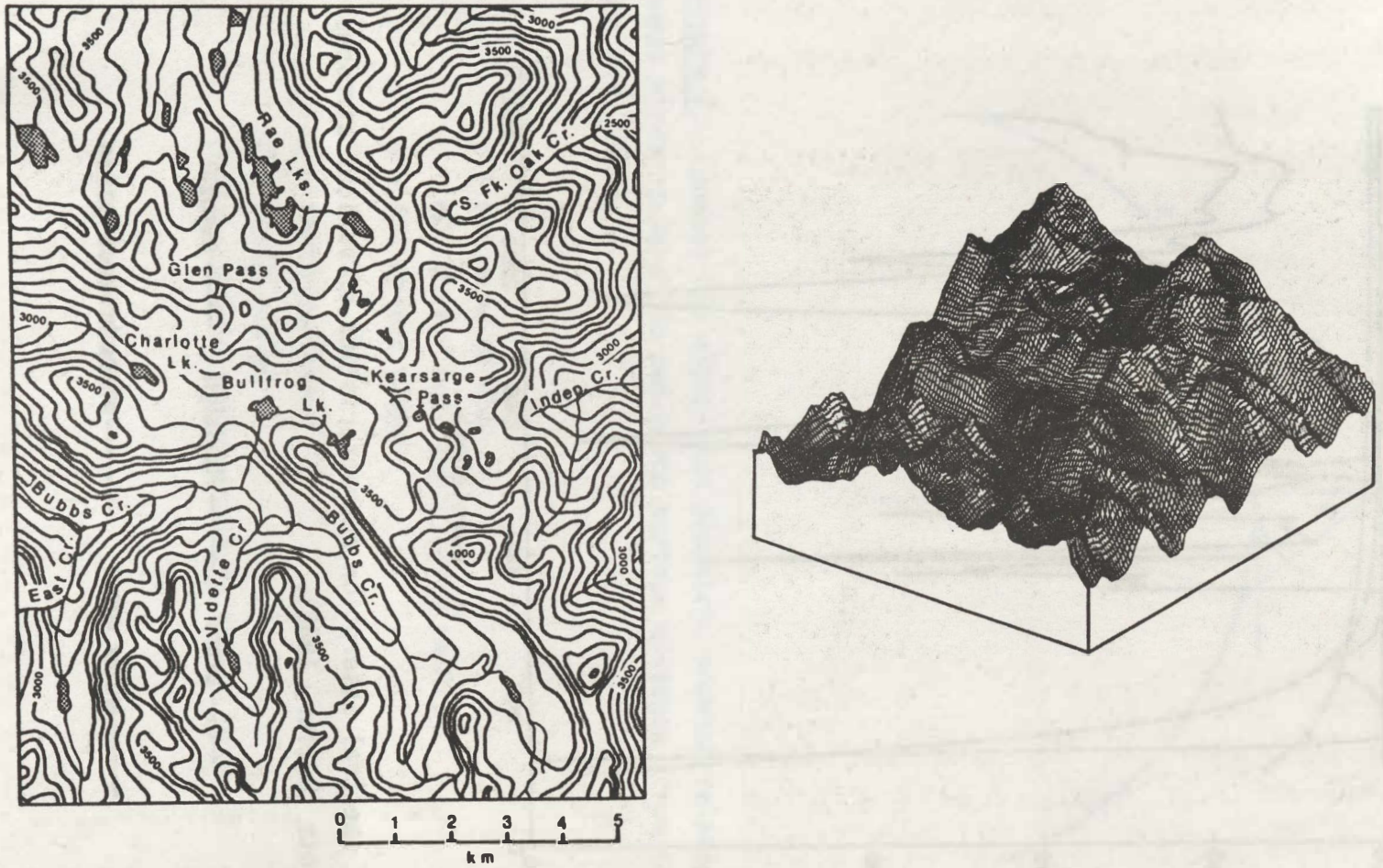

Figure 9: contour map (interval = 100m) and perspective plot (vantage = southeast) of Bullfrog Lake study area, southern Sierra Nevada, California.

Figure 10: pseudo-shaded-relief image of vicinity of Bullfrog Lake study area.

MSS 5 image of vicinity of Bullfrog Lake study area, with corrections for systematic geometric distortions.

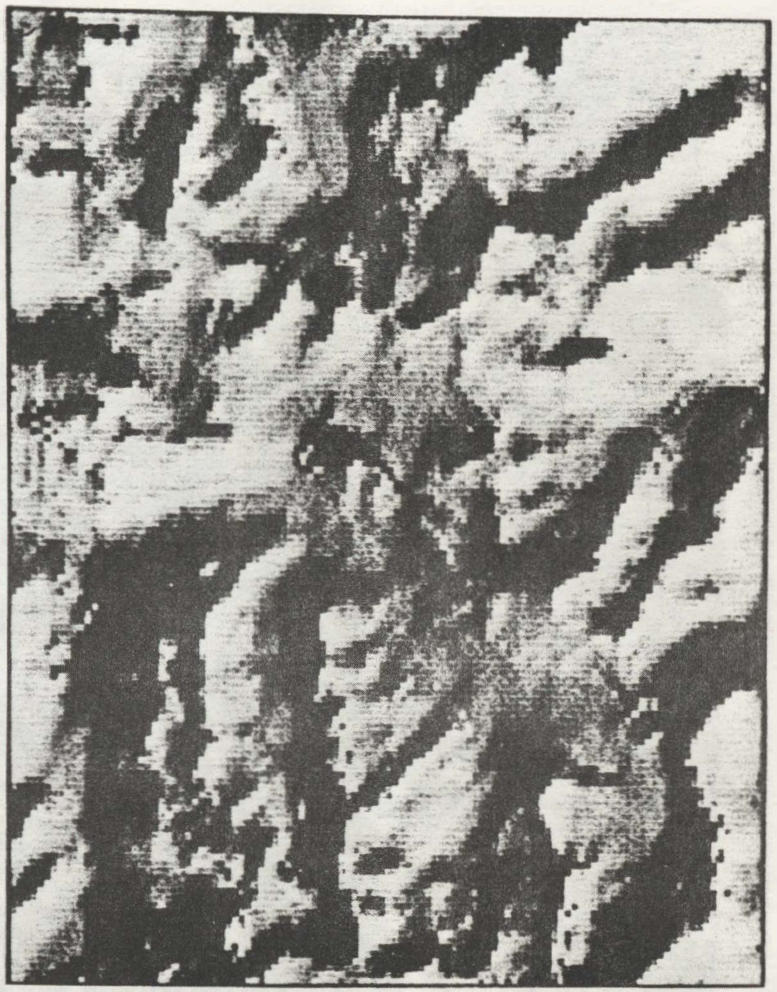

Figure 11: pseudo-shaded-relief image of Bullfrog Lake study area.

MSS 5 image registered to Bullfrog Lake terrain dataset.

Figure 12: image of surface irradiance in MSS band 5, 13 Feb 77, 0937 PST.

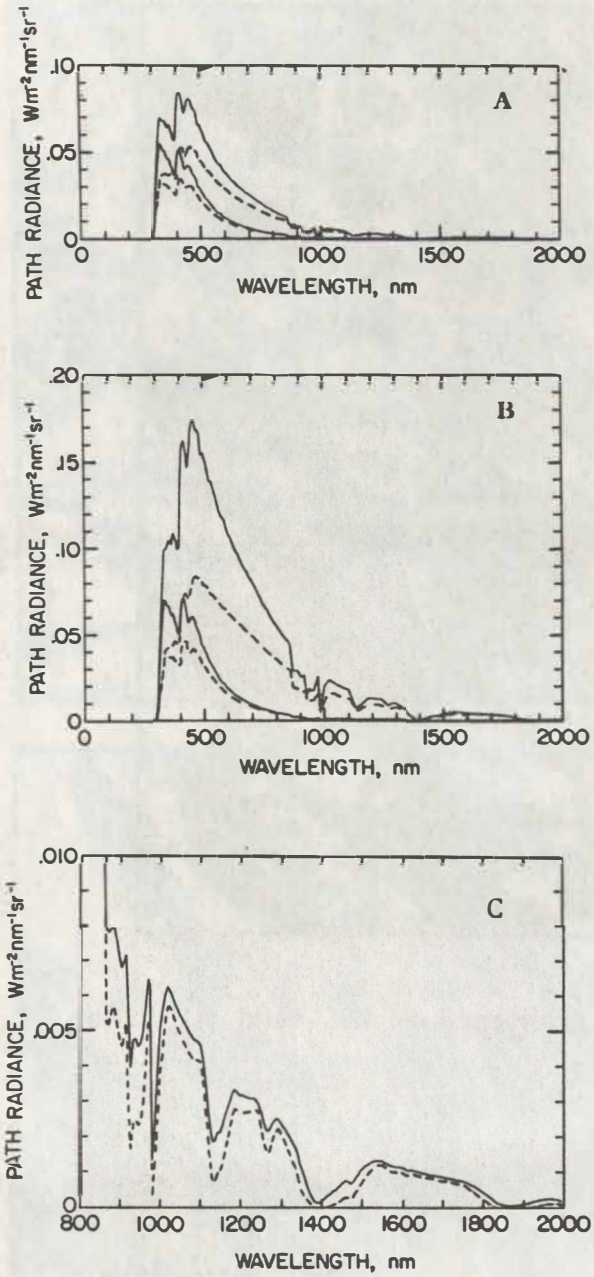

A: elevation 3000 m

B: sea level

A and B

——— : 30 May

- - - : 21 Dec

upper : β = 3500

lower : β = 50

C: sea level; 30 May

——— : 10 mm H_2O

- - - : 40 mm H_2O

Figure 13: sensitivity of path radiance to elevation, solar angle, and atmospheric aerosols. 36.5 deg N latitude, 0937 local time.

Figure 14: image of path radiance levels for Bullfrog Lake study area, 13 Feb 77, 0937 PST.

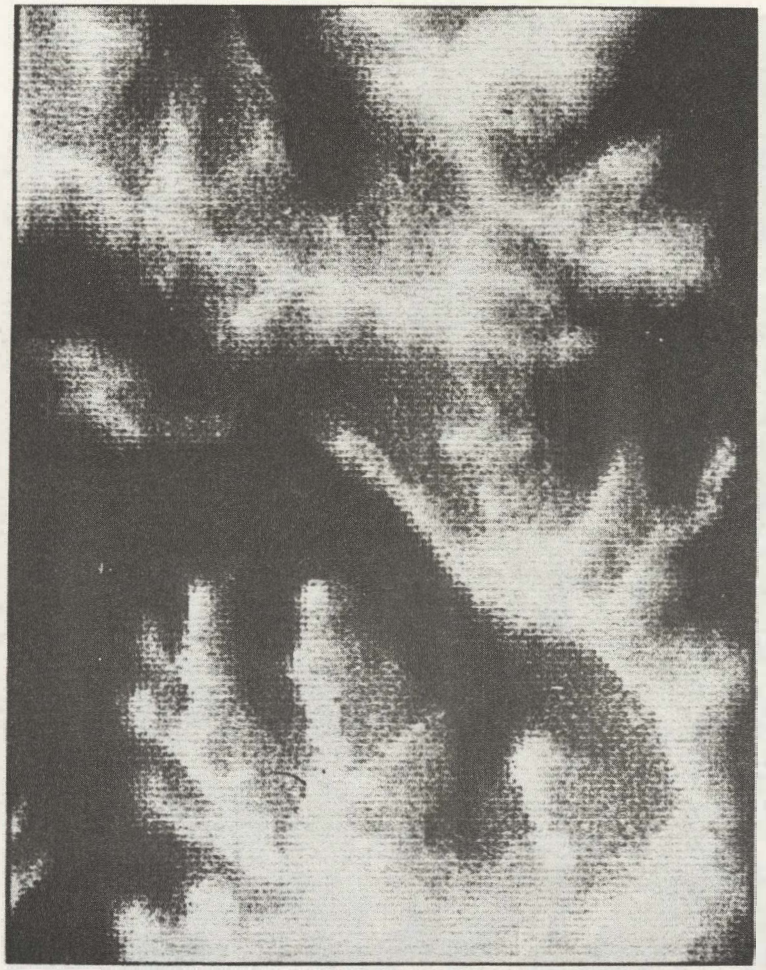

Image of path transmissivity values for Bullfrog Lake study area, 13 Feb 77, 0937 PST.

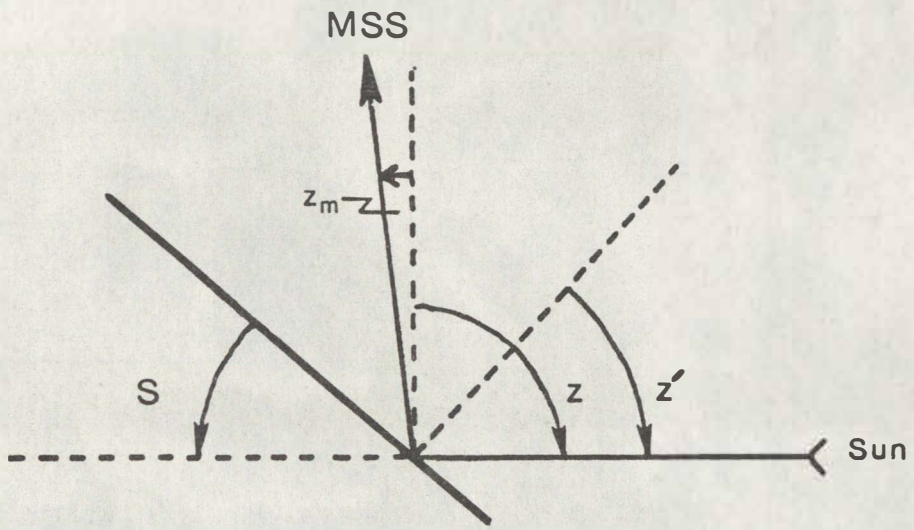

Figure 15: diagram showing lack of specular reflectance component in MSS signal. The angles were chosen to maximize any specular component and represent a "worst case" situation (on edge of MSS frame with sun on horizon).

Parameters

Z_m = maximum apparent zenith angle of MSS (5.78 deg)
Z = maximum possible solar zenith angle (90 deg)
Z' = solar zenith angle relative to slope (47.89 deg)
S = slope, chosen to reflect beam towards MSS (42.11 deg)

From the Fresnel reflectance equation, the Fresnel reflectance under the above conditions is computed to be 0.03. Since this maximum possible value is insignificant, the possibility of the MSS signal being "contaminated" by specular reflectance is discounted.

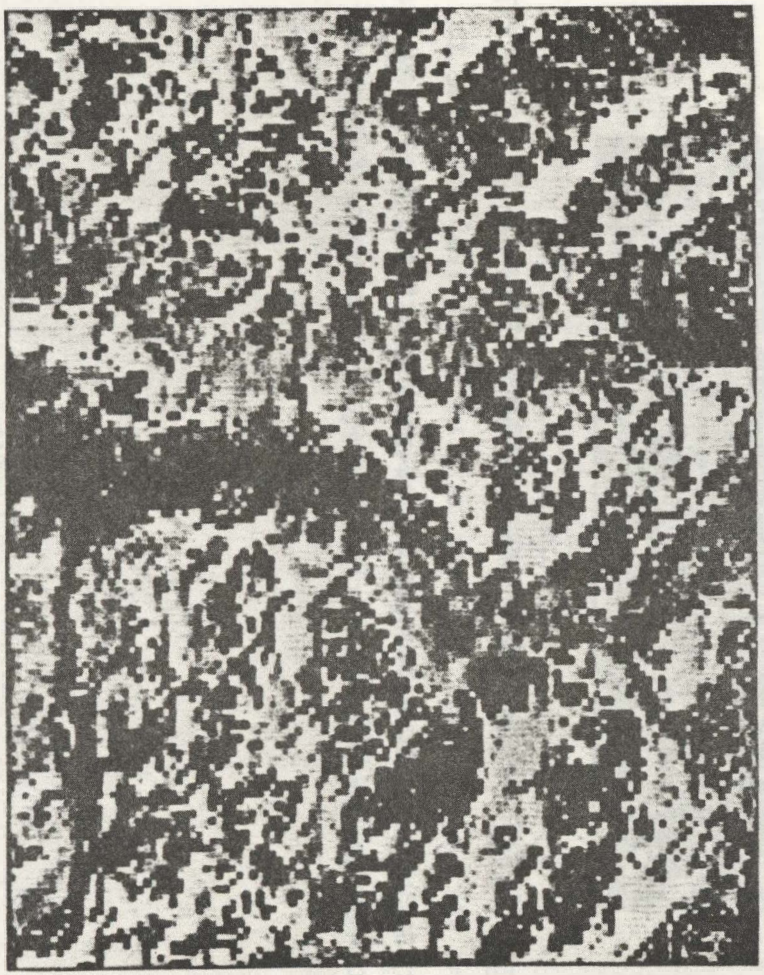

Figure 16: image of ρ' for MSS band 5, Bullfrog Lake study area, 13 Feb 77, 0937 PST.

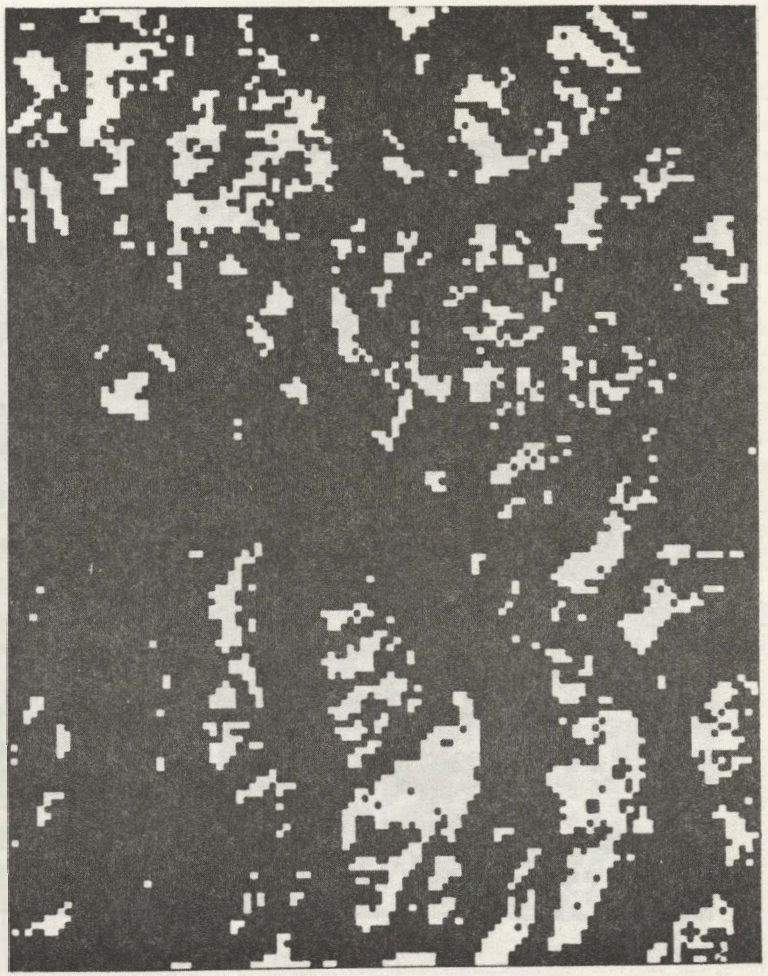

Mask indicating saturated pixels in the original MSS band 5 space radiance image.

Figure 17: image of surface ρ' for MSS band 5, 13 Feb 77, 0937 PST. Locations for which space radiance data were not available due to detector saturation have been assigned values extrapolated from the corresponding ρ' in MSS band 7.

MULTISPECTRAL SCANNER BANDS 4 – 7 (LANDSAT 1)

BAND	MAXIMUM RADIANCE (milliwats cm⁻² – sr)	
	LOW GAIN	HIGH GAIN
4	2.48	0.83
5	2.00	0.67
6	1.76	N A
7	4.00	N A
8[1]		

[1] As Band 8 is a thermal sensor, its response characteristics are not quoted in terms of energy. The relation of sensor response (voltage) to scene-apparent-temperature is being investigated and will be provided when determined.

MULTISPECTRAL SCANNER BANDS 4 – 7 (LANDSAT 2)

BAND	LOW GAIN[1]		HIGH GAIN	
	R Min	R Max	R Min	R Max
4	.10	2.10	.06	.80
5	.07	1.56	.04	.55
6	.07	1.40		
7	.14	4.15		
	LOW GAIN[2]			
4	.08	2.63		
5	.06	1.76		
6	.06	1.52		
7	.11	3.91		

[1] Prior to July 16, 1975
[2] After July 16, 1975

MULTISPECTRAL SCANNER BANDS 4 – 7 (LANDSAT 3)

BANDS	LOW GAIN[1]		HIGH GAIN	
	R Min	R Max	R Min	R Max
4	.04	2.20	.01	.85
5	.03	1.75	.01	.65
6	.03	1.45		
7	.03	4.41		
	LOW GAIN[2]			
4	.04	2.59		
5	.03	1.79		
6	.03	1.49		
7	.03	3.83		

[1] Prior to June 1, 1978
[2] After June 1, 1978

Table 1: Landsat MSS saturation and threshold radiances (only Landsat-3 is currently operational; from U.S. Geological Survey, 1979).

detector	band 4	band 5	band 6	band 7
0	55.4	64.2	63.2	23.2
1	55.8	64.6	63.4	22.7
2	56.6	65.0	64.4	23.3
3	56.8	65.5	64.4	23.3
4	56.0	64.3	64.2	22.8
5	56.0	64.5	63.0	22.9

Table 2: mean radiance numbers (RNs) for all MSS detectors, computed for the uncorrected image from which the registered space radiance data were extracted.

☆U.S. GOVERNMENT PRINTING OFFICE: 1981-340-997/1508